Available online at www.sciencedirect.com

ScienceDirect

International Journal of Solids and Structures 43 (2006) 7571–7592

INTERNATIONAL JOURNAL OF SOLIDS and STRUCTURES

www.elsevier.com/locate/ijsolstr

Response of a thin cylindrical panel with constrained edges

Michael El-Raheb *

ATK Mission Research Corporation, Laguna Hills, CA 92653, United States

Received 13 June 2005; received in revised form 14 February 2006
Available online 22 March 2006

Abstract

Static and transient responses of a thin cylindrical panel constrained from motion along its straight edges and simply supported along its curved edges are treated analytically. Independent of modulus, and for a range of geometric parameters, static deformation along the panel's circumference from a uniform radial pressure exhibits an indentation. This indentation does not appear in transient response of the panel from an impulse of short duration. Extensional boundary constraints strongly affect peak stress in static and transient response.

Keywords: Cylindrical panel; Static stability; Transient response

0. Introduction

Static response, buckling and frequency response of curved panels were treated extensively in the literature. Skvortsov et al. (1998) analyzed static response of a cylindrical panel adopting general shell, shallow shell and curved plate theories, as well as a nonlinear model with arbitrary generator shape. Skvortsov et al. (2000) treated static response and stability of an arbitrary singly curved sandwich panel with general boundary conditions based on the Reissner–Mindlin plate theory. Blevins (1981) adopted Sewall's approximate shallow shell formulation to consider a wide range of boundary conditions. Approximate solutions to free vibration, buckling and transient response of the panel were obtained by Sheinman and Reichman (1992) using the reduced bending stiffness method, and by Chun and Lam (1995) employing the Ritz method with the beam's eigenfunctions or simple admissible polynomials as trial functions. DeRosa and Franciosi (2000) adopted the differential quadrature method to determine the inextensional resonances of thin arcs. All analyses above are based on approximate solutions along the circumferential direction.

Dynamic response of curved panels from a pulse of duration much longer than the panel's fundamental period has been the subject of recent investigations. Among these, Johnson et al. (1984) treated the response of an infinite panel or arc to an eccentric line load. Ramkumar and Thakar (1985) extended the analysis to laminated panels with finite length along the generator and neglected inplane and rotary inertias and shear deformation confining their analysis to quasi-static conditions. The effect of panel geometric imperfection on

* Tel.: +1 626 796 5528; fax: +1 626 583 8834.
E-mail address: mertrident@earthlink.net

0020-7683/$ - see front matter
doi:10.1016/j.ijsolstr.2006.03.015

response was addressed by Kapania and Stoumbos (1994). The effect of impactor contact force on response was studied by Prasad et al. (1994). The nonlinear impact response of thin laminates was studied analytically by Byun and Kapania (1992), and by Ambur et al. (1995). Matsuhashi et al. (1993) investigated the effect of inplane stiffening on linear and nonlinear response of composite panels. Kistler and Waas (1999) performed systematic experiments and finite element analysis on finite cylindrical panels subjected to low velocity impact generating contact forces lasting 12–18 ms. In there study, effects on peak force and displacement of panel curvature and extensional and flexural boundary constraints were parametrized. They concluded that for excitations with long time duration, static and dynamic results are related.

Hardening curved panels to withstand explosive pressure is a design requirement for shielding sensitive equipment from explosive loads. Some applications are further constrained by geometric distortion from static and dynamic pressures. Analysis of these applications relies mostly on general-purpose finite element computer programs. A comparison of results from these numerical models with an independent analysis is needed to validate results and provide insight into the physics of the problem that may not be gained from a purely numerical model. For transient phenomena following external loads of short duration, one simulation may take several hours on a fast workstation. To quickly validate results from these laborious models, engineers tend to simplify geometry and properties by considering limiting cases. Understanding the validity of these approximations is necessary since comparing results from a purely numerical model with narrowly valid approximations may lead to more uncertainty in the results. An overly simplified model does not always yield a valid result, yet a complicated numerical model needs consistent verification. The middle ground of an analysis that is neither a "black box" nor overly simplified helps validate trends and, most importantly, provide understanding. Balancing the degree of simplification by including realistic physical effects in the analytical model rapidly increases its mathematical complexity.

The present analysis addresses static response and stability of a cylindrical panel to a uniform radial pressure, and transient response to a blast-generated impulsive pressure of short rise time and duration lasting 0.3 ms. The impulsive load excites shorter wavelength modes than those in all references above. In turn, the wave propagation aspects of the panel dominate response soon after impulse. The relationship between quasi-static and dynamic response is investigated.

Section 1 solves the linear dynamic equations of the finite panel. The axial dependence is eliminated assuming simple supports along the panel's circular edges. Note that solutions for each axial wave number m are uncoupled meaning that each m is associated to an infinite set of circumferential wave numbers n. The constant coefficients of the governing equations allow an analytical solution along θ in terms of exponentials. The exponents determined from the dispersion relation are complex numbers $\alpha_r + \hat{\imath}\alpha_i$ where $\hat{\imath} = \sqrt{-1}$. The imaginary part α_i represents a propagation wave number and the real part α_r represents an evanescent wave number with contributions only within short intervals near the two boundaries of the panel along θ. These intervals are known as flexural boundary layers where boundary constraints are enforced. α_r is a frequency dependent number that reaches large magnitudes producing round-off error when terms like $(1 - e^{|\alpha_r \theta_l|})$ are evaluated where θ_l is angle sustained by the arc. To reduce the error, θ_l is divided into m_s constant intervals $\Delta\theta = \theta_l/m_s$ so that $e^{|\alpha_r \Delta\theta|}$ is within machine precision. To solve the problem of a panel segmented along θ, transfer matrices relating state vectors at the two ends of a segment are derived. Continuity of the state vectors at interfaces of segments and boundary conditions at the two ends yields sufficient equations in the unknown state vectors. In fact, the same method applies to a panel with material inhomogeneity along θ. Moreover, boundary conditions are satisfied exactly without the need of approximating displacement functions by beam-type modes, a common simplification in most references.

Section 2 addresses the infinite panel or arc. Segmenting the arc along the circumference follows the same procedure adopted for the finite panel. Section 3 discusses static response and stability followed by transient response of the panel and arc. Of particular interest is the effectiveness of extensional boundary conditions on magnitude of static and transient stresses.

1. Finite cylindrical panel

For a finite cylindrical panel, Fig. 1 shows displacements u, v, w, and stress resultants for inplane N_{xx}, $N_{\theta\theta}$, $N_{x\theta}$, moment M_{xx}, $M_{\theta\theta}$, $M_{x\theta}$, and shear Q_x, Q_θ in a cylindrical element. The dynamic equations are

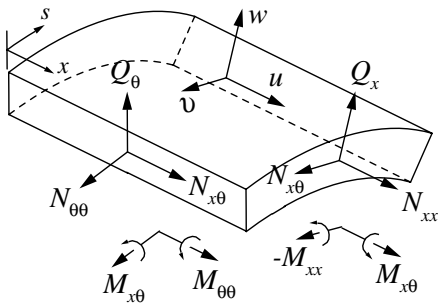

Fig. 1. Displacements and stress resultants of cylindrical element.

$$
\begin{aligned}
&D_{11}(u)+D_{12}(v)+D_{13}(w)=0\\
&D_{21}(u)+D_{22}(v)+D_{23}(w)=0\\
&D_{31}(u)+D_{32}(v)+D_{33}(w)=p_w(x,\theta)f_w(t)
\end{aligned}
\tag{1a}
$$

$$
\begin{aligned}
&D_{11}=N_0(\partial_{xx}+(1-v)\partial_{\theta\theta}/2R^2)-\rho h\partial_{tt}\\
&D_{12}=D_{21}=N_0(1+v)\partial_{x\theta}/2R\\
&D_{13}=D_{31}=-N_0v\partial_x/R
\end{aligned}
\tag{1b}
$$

$$
\begin{aligned}
&D_{22}=N_0((1-v)/2\partial_{xx}+\partial_{\theta\theta}/R^2)+M_0/R^2(\partial_{\theta\theta}/R^2+2(1-v)\partial_{xx})-(1+\chi\tilde{r}^2)\rho h\partial_{tt}\\
&D_{23}=D_{32}=-N_0\partial_\theta/R^2+M_0\partial_\theta(\partial_{\theta\theta}/R^2+(2-v)\partial_{xx})/R^2+\rho h\chi\tilde{r}^2\partial_{\theta tt}\\
&D_{33}=M_0\nabla^4+N_0/R^2+\rho h(1-\chi\tilde{r}^2R^2\nabla^2)\partial_{tt}
\end{aligned}
\tag{1c}
$$

$$
\begin{aligned}
&N_0=Eh/(1-v^2),\quad M_0=Eh^3/12(1-v^2)\\
&\nabla^2=\partial_{xx}+\partial_{\theta\theta}/R^2,\quad \nabla^4=\nabla^2\nabla^2,\quad \tilde{r}=h/(\sqrt{12}R)\\
&0\leqslant x\leqslant l_x,\quad 0\leqslant\theta\leqslant\theta_l,\quad \theta_l=l_s/R
\end{aligned}
\tag{1d}
$$

θ is circumferential coordinate, x is axial coordinate, l_x is panel length along x and l_s is arc length along θ where the arc sustains an angle θ_l, (R,h) are cylinder mean radius and thickness, (ρ,E,v) are mass density, modulus and Poisson ratio, t is time, and $p_w(x,\theta)$ and $f_w(t)$ are spatial and time dependence of the applied normal pressure. The shear deformation factor χ is derived in El-Raheb (2006). The constitutive relations are

$$
\begin{aligned}
&N_{xx}=N_0(\partial_x u+v(\partial_\theta v-w)/R)\\
&N_{\theta\theta}=N_0(v\partial_x u+(\partial_\theta v-w)/R)\\
&N_{x\theta}=(1-v)N_0(\partial_\theta u/R+\partial_x v)/2
\end{aligned}
\tag{2a}
$$

$$
\begin{aligned}
&M_{xx}=-M_0(\partial_{xx}w+v(\partial_{\theta\theta}w+\partial_\theta v)/R^2)\\
&M_{\theta\theta}=-M_0(v\partial_{xx}w+(\partial_{\theta\theta}w+\partial_\theta v)/R^2)\\
&M_{x\theta}=(1-v)M_0(\partial_{x\theta}w+\partial_x v)/R
\end{aligned}
\tag{2b}
$$

$$
\begin{aligned}
&Q_x=\partial_x M_{xx}+\rho h^3\chi\partial_{xtt}w/12\\
&Q_\theta=\partial_\theta M_{\theta\theta}/R-2\partial_x M_{x\theta}+\rho hR\tilde{r}^2\chi(\partial_{\theta tt}w+\partial_{tt}v)
\end{aligned}
\tag{2c}
$$

Stresses are related to stress resultants by

$$
\begin{aligned}
&\sigma_{xxe}=N_{xx}/h,\quad \sigma_{\theta\theta e}=N_{\theta\theta}/h \qquad \text{extensional}\\
&\sigma_{xxf}=6M_{xx}/h^2,\quad \sigma_{\theta\theta f}=6M_{\theta\theta}/h^2 \qquad \text{flexural}\\
&\tau_{xx}=1.5Q_x/h,\quad \tau_{\theta\theta}=1.5Q_\theta/h \qquad \text{shear}
\end{aligned}
\tag{2d}
$$

For simply supported boundary conditions (SS1) at $x = 0$ and $x = l_x$

$$v = w = N_{xx} = M_{xx} = 0 \tag{3}$$

Eq. (12a) then admit a solution in terms of exponentials along θ and trigonometric functions along x

$$u(x,\theta,t) = \sum_{m=1}\sum_{k=1}^{8} u_{km} e^{\alpha_{km}\theta} C_m(x) e^{\hat{i}\omega t} \tag{4a}$$

$$v(x,\theta,t) = \sum_{m=1}\sum_{k=1}^{8} v_{km} e^{\alpha_{km}\theta} S_m(x) e^{\hat{i}\omega t} \tag{4b}$$

$$w(x,\theta,t) = \sum_{m=1}\sum_{k=1}^{8} w_{km} e^{\alpha_{km}\theta} S_m(x) e^{\hat{i}\omega t} \tag{4c}$$

$$S_m(x) = \sin(k_{xm}x), \quad C_m(x) = \cos(k_{xm}x), \quad k_{xm} = m\pi/l_x$$

Substituting (4a)–(4c) in (1a) noting that $S_m(x)$, $C_m(x)$ are orthogonal yields an 8th order polynomial in the complex exponents α_{km} for each m

$$\sum_{k=0}^{4} c_{km}\alpha_{km}^{2k} = 0 \tag{5}$$

The expressions for c_{km} are lengthy and will be omitted for shortness. u_{km} and v_{km} are determined by substituting (4a)–(4c) in the first two equations of (1a), setting $w_{km} = 1$ without loss of generality, and equating coefficients of $e^{\alpha_{km}\theta}$ to zero

$$\begin{bmatrix} L_{11,km} & L_{12,km} \\ L_{21,km} & L_{22,km} \end{bmatrix} \begin{Bmatrix} u_{km} \\ v_{km} \end{Bmatrix} = -\begin{Bmatrix} L_{13,km} \\ L_{23,km} \end{Bmatrix} \tag{6a}$$

$$\begin{aligned} L_{11,km} &= N_0(-k_{xm}^2 + (1-\nu)\alpha_{km}^2/2R^2) + \rho h\omega^2 \\ L_{12,km} &= -L_{21,km} = N_0(1+\nu)k_{xm}\alpha_{km}/2R, \quad L_{13,km} = -N_0\nu k_{xm}/R \\ L_{22,km} &= N_0(-(1-\nu)k_{xm}^2/2 + \alpha_{km}^2/R^2) + M_0/R^2(-2(1-\nu)k_{xm}^2 + \alpha_{km}^2/R^2) + (1+\chi\tilde{r}^2)\rho h\omega^2 \\ L_{23,km} &= (-N_0 + M_0\alpha_{km}^2/R^2)\alpha_{km}/R^2 - \rho h\chi\tilde{r}^2\omega^2 \end{aligned} \tag{6b}$$

For a complete cylinder, all α_{km} are imaginary integers representing circumferential wave numbers. Fig. 2(a1)–(d1) plots a typical distribution of the three types of α's for $m = 3$, and Fig. 2(a2)–(d2) plots the α's for $m = 11$. Note that the largest real part $\alpha_{re} \sim 40$ at $\Omega = 20$ kHz and rises with Ω and m. Complex conjugates appear only for frequencies below cut-off $\Omega_{co,m}$ of a particular m. For example, $\Omega_{co,3} \sim 1.5$ kHz (Fig. 2(d1)), and $\Omega_{co,11} \sim 3.3$ kHz (Fig. 2(d2)). For frequencies high compared to $\Omega_{co,m}$, arithmetic accuracy suffers from round-off error because of the large $|\mathrm{Re}(\alpha_k)|$. This difficulty can be circumvented by dividing the arc $0 \leqslant \theta \leqslant \theta_l$ into m_s segments $\theta_j \leqslant \theta \leqslant \theta_{j+1}$, $1 \leqslant j \leqslant m_s + 1$ where $\theta_1 = 0$ and $\theta_{m_s+1} = \theta_l$. For each segment a term like $e^{|\alpha_k(\theta_{j+1}-\theta_j)|}$ is smaller in magnitude since $\theta_{j+1} - \theta_j = \theta_l/m_s \ll \theta_l$. For a segmented arc the transfer matrix method is employed. Divide the panel's surface into axial strips within the interval $0 \leqslant \theta \leqslant \theta_l$ into m_s segments $\theta_j \leqslant \theta \leqslant \theta_{j+1}$, $1 \leqslant j \leqslant m_s + 1$ where $\theta_1 = 0$ and $\theta_{m_s+1} = \theta_l$. Substituting(3) in (2a) and defining

$$\mathbf{f}_{jm} = \{N_{\theta\theta}, N_{x\theta}, Q_\theta, M_{\theta\theta}\}_{jm}^{\mathrm{T}}, \quad \mathbf{g}_{jm} = \{u, v, w, w_\theta\}_{jm}^{\mathrm{T}} \tag{7a}$$

yields

$$\mathbf{f}_{jm} = \mathbf{B}_{fjm}\mathbf{C}_{jm}, \quad \mathbf{g}_{jm} = \mathbf{B}_{gjm}\mathbf{C}_{jm} \tag{7b}$$

$\mathbf{C}_{jm} = \{C_{1j}, C_{2j}, \ldots, C_{8j}\}_m^{\mathrm{T}}$, $\mathbf{B}_{fjm}$ and $\mathbf{B}_{gjm}$ are 4×8 matrices with coefficients involving the exponential functions in (4) and their derivatives. Defining the state vector at an interface as $\mathbf{S}_{jm} = \{\mathbf{f}_j, \mathbf{g}_j\}_m^{\mathrm{T}}$, evaluating (7b) at the two ends of segment j then eliminating $\mathbf{C}_{jm}$ determines the transfer matrix of the jth segment relating $\mathbf{S}_{jm}(\theta_j)$ to $\mathbf{S}_{jm}(\theta_{j+1})$

$$\begin{aligned} &\mathbf{S}_{jm}(\theta_{j+1}) = \mathbf{T}_{(j,j+1)m}\mathbf{S}_{jm}(\theta_j) \equiv \mathbf{B}_{sjm}^{-1}(\theta_j)\mathbf{B}_{sjm}(\theta_{j+1})\mathbf{S}_{jm}(\theta_j) \\ &\mathbf{B}_{sjm} = \begin{bmatrix} \mathbf{B}_{fjm} \\ \mathbf{B}_{gjm} \end{bmatrix} \end{aligned} \tag{8}$$

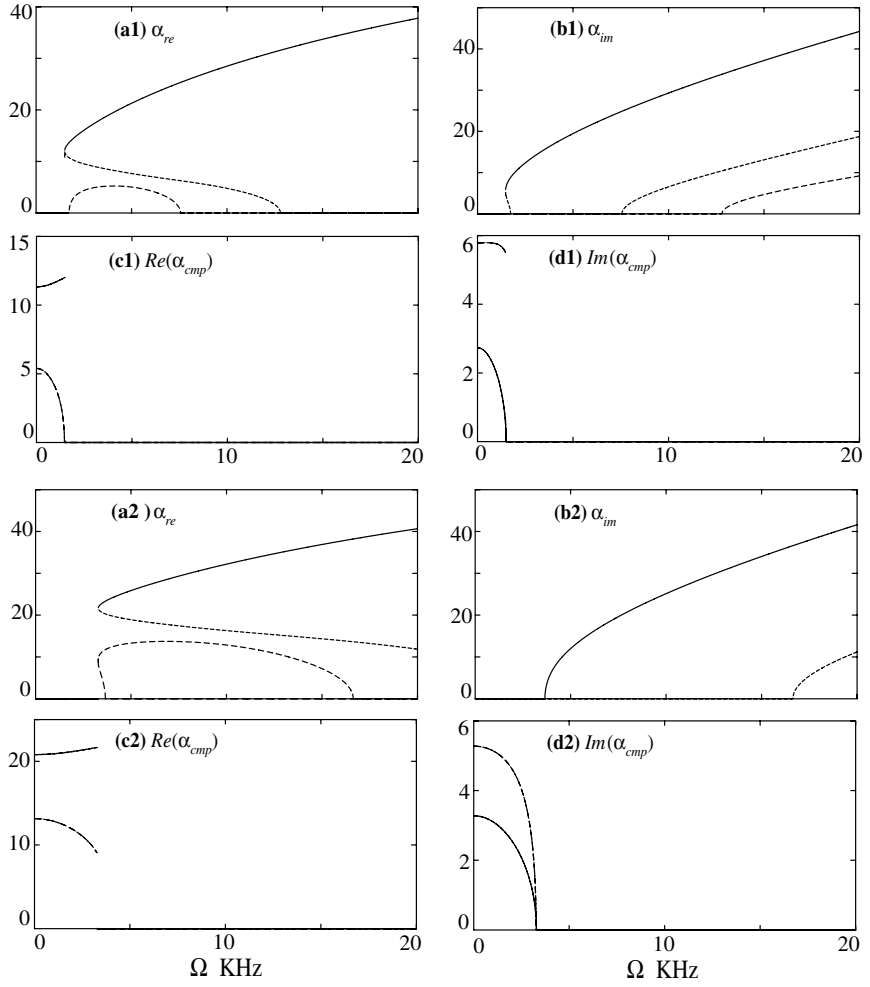

Fig. 2. Characteristic exponents; $R = 50$ cm, $h = 1.27$ cm, $l_s = l_x = 100$ cm. (a1)–(d1) $m = 3$ and (a2)–(d2) $m = 11$.

Enforcing continuity of $\mathbf{f}_{jm}$ and $\mathbf{g}_{jm}$ at interfaces of segments and boundary conditions at $\theta = 0$ and $\theta = \theta_l$ produces a set of $m_s + 1$ tri-diagonal block matrices in the interface state vectors $\mathbf{S}_{jm}$. For the case of three segments, the tri-diagonal block system takes the form

$$\begin{bmatrix} \mathbf{F}_a & \mathbf{G}_a & \mathbf{0} & \mathbf{0} & & & & \\ \mathbf{t}_{11,1} & \mathbf{t}_{12,1} & -\mathbf{I} & \mathbf{0} & & & & \\ \mathbf{t}_{21,1} & \mathbf{t}_{22,1} & \mathbf{0} & -\mathbf{I} & \mathbf{0} & \mathbf{0} & & \\ \mathbf{0} & \mathbf{0} & \mathbf{t}_{11,2} & \mathbf{t}_{12,2} & -\mathbf{I} & \mathbf{0} & & \\ & & \mathbf{t}_{21,2} & \mathbf{t}_{22,2} & \mathbf{0} & -\mathbf{I} & \mathbf{0} & \mathbf{0} \\ & & \mathbf{0} & \mathbf{0} & \mathbf{t}_{11,3} & \mathbf{t}_{12,3} & -\mathbf{I} & \mathbf{0} \\ & & & & \mathbf{t}_{21,3} & \mathbf{t}_{22,3} & \mathbf{0} & -\mathbf{I} \\ & & & & \mathbf{0} & \mathbf{0} & \mathbf{F}_b & \mathbf{G}_b \end{bmatrix}_m \begin{Bmatrix} \mathbf{f}_1 \\ \mathbf{g}_1 \\ \mathbf{f}_2 \\ \mathbf{g}_2 \\ \mathbf{f}_3 \\ \mathbf{g}_3 \\ \mathbf{f}_4 \\ \mathbf{g}_4 \end{Bmatrix}_m = \begin{Bmatrix} \mathbf{0} \\ \mathbf{p}_1 \\ \mathbf{0} \\ \mathbf{p}_2 \\ \mathbf{0} \\ \mathbf{0} \\ \mathbf{0} \\ \mathbf{0} \end{Bmatrix}_m \tag{9}$$

$$\begin{bmatrix} \mathbf{t}_{11} & \mathbf{t}_{12} \\ \mathbf{t}_{21} & \mathbf{t}_{22} \end{bmatrix}_{jm} = \mathbf{T}_{(j,j+1)m}$$

$\mathbf{F}_a$, $\mathbf{G}_a$ and $\mathbf{F}_b$, $\mathbf{G}_b$ are 4×4 matrices expressing boundary conditions at $\theta=0$ and $\theta=\theta_l$, and $\mathbf{I}$ and $\mathbf{0}$ are 4×4 unit and null matrices. Re-write the tri-diagonal system as

$$\mathbf{T}_{\mathrm{G}m}\mathbf{S}_{\mathrm{G}m}=\mathbf{P}_m \tag{10}$$

$\mathbf{T}_{\mathrm{G}m}$ is the global transfer matrix and $\mathbf{S}_{\mathrm{G}m}=\{\mathbf{S}_1,\mathbf{S}_2,\ldots,\mathbf{S}_j,\ldots,\mathbf{S}_{m_s+1}\}_m^{\mathrm{T}}$ is the global state vector formed of the ensemble of all interface state vectors and $\mathbf{P}_m=\{\mathbf{0},\mathbf{p}_1,\mathbf{0},\mathbf{p}_2,\ldots,\mathbf{0},\mathbf{p}_{m_s-2},\mathbf{0},\mathbf{0},\mathbf{0},\mathbf{0}\}^{\mathrm{T}}$ is the external excitation vector. The homogeneous form of (9) yields the eigenvalue problem

$$\det|\mathbf{T}_{\mathrm{G}m}|=0 \tag{11}$$

and the eigenset $\{\mathbf{\Phi}_{nm},\omega_{nm}\}$ with $\mathbf{\Phi}_{nm}=\{\boldsymbol{\phi}_1,\boldsymbol{\phi}_2,\ldots,\boldsymbol{\phi}_j,\ldots,\boldsymbol{\phi}_{m_s}\}_{nm}^{\mathrm{T}}$, $\boldsymbol{\phi}_{j,nm}=\{\varphi,\eta,\zeta\}_{j,n\,m}$ with components φ, η, ζ related to u, v, w, being the nth modal displacement eigenvector of the jth segment with axial wave number m.

Transient response is determined by expanding the global displacement vectors $\mathbf{G}_{\mathrm{G}}=\{\bar{\mathbf{g}}_1,\bar{\mathbf{g}}_2,\ldots,\bar{\mathbf{g}}_j,\ldots,\bar{\mathbf{g}}_{m_s}\}^{\mathrm{T}}$ in their eigenfunctions where $\bar{\mathbf{g}}_j=\{u,v,w\}_j^{\mathrm{T}}$

$$\begin{aligned}&\mathbf{G}_{\mathrm{G}}=\sum_n\sum_m a_{nm}(t)\mathbf{\Phi}_{nm}(\theta)\mathbf{\Psi}_m(x)\\&\mathbf{\Psi}_m(x)=\{C_m(x),S_m(x),S_m(x),S_m(x)\}^{\mathrm{T}}\end{aligned} \tag{12}$$

Substituting (12) in (1a) and enforcing orthogonality of the eigenfunctions produces uncoupled ordinary differential equations in the generalized coordinates $a_{nm}(t)$

$$\begin{aligned}&\ddot{a}_{nm}(t)+\omega_{nm}^2a_{nm}(t)=-N_{fn,m}/N_{nn,m}\\&N_{fn,m}=\langle\mathbf{\Phi}_{nm}|\mathbf{p}\rangle,\\&N_{nn,m}=0.5\rho hRl_x\int_0^{\theta_l}(\varphi_{nm}^2+\eta_{nm}^2+\zeta_{nm}^2+\tilde{r}^2\chi((Rk_{xm}\zeta_{nm})^2+(\partial_\theta\zeta_{nm}-\eta_{nm})^2))\mathrm{d}\theta\\&\mathbf{p}=\{0,0,p_w(x,\theta)\}^{\mathrm{T}}\end{aligned} \tag{13}$$

ω_{nm} is the eigenfrequency of the (nm)th mode.

2. Arc or infinite cylindrical panel

In the case of an infinite cylindrical panel, axial dependence vanishes meaning that the dependent variables $u=N_{xx}=N_{x\theta}=M_{xx}=M_{x\theta}=Q_{xx}=0$. In terms of displacements the dynamic equations are

$$\begin{aligned}&D_{22}(v)+D_{23}(w)=0\\&D_{32}(v)+D_{33}(w)=p_w(\theta)f_w(t)\\&0\leqslant\theta\leqslant\theta_l,\quad\theta_l=l_s/R\end{aligned} \tag{14a}$$

$$\begin{aligned}&D_{22}=N_0\partial_{\theta\theta}/R^2+M_0\partial_{\theta\theta}/R^4-(1+\chi\tilde{r}^2)\rho h\partial_{tt}\\&D_{23}=D_{32}=-N_0\partial_\theta/R^2+M_0\partial_{\theta\theta\theta}/R^4+\rho h\chi\tilde{r}^2\partial_{\theta tt}\\&D_{33}=M_0\partial_{\theta\theta\theta\theta}/R^4+N_0/R^2+\rho h(1-\chi\tilde{r}^2\partial_{\theta\theta})\partial_{tt}\\&N_0=Eh/(1-\nu^2),\quad M_0=Eh^3/12(1-\nu^2)\\&\tilde{r}=h/(\sqrt{12}R),\quad\chi=1+2/\kappa(1-\nu),\quad\kappa=\pi^2/12\end{aligned} \tag{14b}$$

κ is Mindlin's shear constant (Mindlin, 1951). The constitutive relations are

$$\begin{aligned}&N_{\theta\theta}=N_0(\partial_\theta v-w)/R\\&M_{\theta\theta}=-M_0(\partial_{\theta\theta}w+\partial_\theta v)/R^2\\&Q_\theta=\partial_\theta M_{\theta\theta}/R+\rho hR\tilde{r}^2\chi(\partial_{\theta tt}w+\partial_{tt}v)\end{aligned} \tag{15}$$

Since Eq. (14a) have constant coefficients, they admit a solution in terms of exponentials. For harmonic motions in time with radian frequency ω

$$v(\theta,t)=\sum_{k=1}^{6} v_k e^{\alpha_k\theta}e^{\hat{i}\omega t},\quad w(\theta,t)=\sum_{k=1}^{6} w_k e^{\alpha_k\theta}e^{\hat{i}\omega t} \tag{16}$$

Substituting (16) in (14a) yields the 6th order polynomial in the complex exponents α_k

$$\sum_{k=0}^{3} c_k\alpha^{2k}=0 \tag{17}$$

$$c_3=N_0M_0/R^6,\quad c_2=\rho h\omega^2(N_0\chi^2+M_0/R^2)/R^2+2N_0M_0/R^6$$
$$c_1=\rho h\omega^2(-M_0/R^4+\rho h\omega^2\chi^2-N_0(1-2\chi^2)/R^2)/R^2+N_0M_0/R^6$$
$$c_0=\rho h\omega^2(1+\chi^2)(N_0/R^2-\rho h\omega^2)$$

Substituting (16) in (15) and defining

$$\mathbf{f}_j=\{N_{\theta\theta},Q_\theta,M_{\theta\theta}\}_j^{\mathrm{T}},\quad \mathbf{g}_j=\{v,w,w_\theta\}_j^{\mathrm{T}} \tag{18a}$$

yields

$$\mathbf{f}_j=\mathbf{B}_{\mathbf{f}j}\mathbf{C}_j,\quad \mathbf{g}_j=\mathbf{B}_{\mathbf{g}j}\mathbf{C}_j \tag{18b}$$

$\mathbf{C}_j=\{C_{1j},C_{2j},\ldots,C_{6j}\}^{\mathrm{T}}$, $\mathbf{B}_{\mathbf{f}j}$ and $\mathbf{B}_{\mathbf{g}j}$ are 3×6 matrices with coefficients involving the exponential functions in (16) and their derivatives. Defining the state vector at an interface as $\mathbf{S}_j=\{\mathbf{f}_j,\mathbf{g}_j\}^{\mathrm{T}}$, evaluating (18b) at the two ends of segment j then eliminating $\mathbf{C}_j$ determines the transfer matrix of the jth segment relating $\mathbf{S}_j(\theta_j)$ to $\mathbf{S}_j(\theta_{j+1})$

$$\mathbf{S}_j(\theta_{j+1})=\mathbf{T}_{j,j+1}\mathbf{S}_j(\theta_j)\equiv\mathbf{B}_{\mathbf{s}j}^{-1}(\theta_j)\mathbf{B}_{\mathbf{s}j}(\theta_{j+1})\mathbf{S}_j(\theta_j)$$
$$\mathbf{B}_{\mathbf{s}j}=\begin{bmatrix}\mathbf{B}_{\mathbf{f}j}\\ \mathbf{B}_{\mathbf{g}j}\end{bmatrix} \tag{19}$$

Enforcing continuity of $\mathbf{f}_j$ and $\mathbf{g}_j$ at interfaces of segments and boundary conditions at $\theta=0$ and $\theta=\theta_l$ produces a set of m_s+1 tri-diagonal block matrices in the interface state vectors $\mathbf{S}_j$. For the case of 3 arc segments, the tri-diagonal block system takes the form of (9) where $\mathbf{F}_a$, $\mathbf{G}_a$ and $\mathbf{F}_b$, $\mathbf{G}_b$ are $3\times$ 3 matrices expressing boundary conditions at $\theta=0$ and $\theta=\theta_l$, and $\mathbf{I}$ and $\mathbf{0}$ are $3\times$ 3 unit and null matrices. From there on, all steps that led the solution of transient response of the finite panel in Section 1 (i.e. Eqs. (10)–(13)) are identical except for the order of matrices and vectors.

3. Results

Some notations and definitions are presented first to facilitate discussing the results to follow. The cylindrical panel has four edges; two edges are circular at $x=0$ and $x=l_x$, and the other two edges are straight along generators at $s=0$ and $s=l_s=R\theta_l$ where s is intrinsic coordinate along the arc length. Symbols bc_x and bc_s will denote boundary conditions along the curved and straight edges, respectively. Since the functions $S_m(x)$, $C_m(x)$ in (4c) satisfy the classical simple supports SS1 defined by

$$bc_x\text{:SS1}\ \Rightarrow\ N_{xx}=v=w=M_{xx}=0;\quad x=0,l_x \tag{20a}$$

this boundary condition will be used throughout the analysis and only reference to bc_s will be made. The following choices will be used for bc_s:

$$bc_s\text{:SS2}\ \Rightarrow\ u=v=w=M_{\theta\theta}=0;\quad s=0,l_s \tag{20b}$$
$$bc_s\text{:SS3}\ \Rightarrow\ u=N_{\theta\theta}=w=M_{\theta\theta}=0;\quad s=0,l_s \tag{20c}$$

The difference between SS2 and SS3 is the constraint on circumferential displacement v that affects the panel's extensional stiffness. The flexural constraint $M_{\theta\theta} = 0$ or $\partial_\theta w = 0$ is of secondary importance when R/h is large. All panels are made of steel with properties

$$E = 2 \times 10^{12}\ \text{dyn/cm}^2, \quad \rho = 8\ \text{g/cm}^3, \quad \nu = 0.3$$

Results are presented in four sub-sections.

Section 3.1 compares resonances of deep arcs from the analysis in Section 2 to those of DeRosa and Franciosi (2000), Section 3.2 discusses static response, Section 3.3 discusses static stability, and Section 3.4 discusses transient response to impulse of short duration.

3.1. Comparison of arc resonances

Resonances of deep arcs from the present analysis are compared to those reported by DeRosa and Franciosi (2000) since they treat three different boundary conditions and list sufficient resonances for an acceptable validation. One concern is that their method is restricted to inextensional motion which from Eq. (15) implies that $\varepsilon_{\theta\theta,e} \equiv \partial_\theta v - w = 0 \Rightarrow \partial_\theta v = w$. A consequence of this assumption is that $N_{\theta\theta} \approx \partial_\theta Q_\theta + R\rho\partial_{tt} w$ instead of the expression in (15). The non-dimensional resonance defined in the reference as $\widetilde{\Omega}_n = \sqrt{12}\omega_n R^2/(c_\sigma h)$ will be used in the comparison, where ω_n is the nth resonance and $c_\sigma = \sqrt{E/\rho(1-\nu^2)}$ is speed of sound in plane-stress. Table 1 lists $\widetilde{\Omega}_n$'s for $1 \leqslant n \leqslant 10$ when $\theta_l = \pi$ (half circle) and $R/h = 80$ to meet the thinness condition. At the arc's edges, three boundary conditions were considered: (i) clamped/clamped ($v \equiv w \equiv \partial_\theta w = 0$), (ii) hinged/hinged ($v \equiv w \equiv M_{\theta\theta} = 0$), and (iii) cantilever or clamped/free, where the free condition means $N_{\theta\theta} \equiv Q_\theta \equiv M_{\theta\theta} = 0$.

For cases (i) and (ii), the difference in corresponding $\widetilde{\Omega}_n$'s does not exceed 0.4%. In contrast, for case (iii), the first resonance is 50% lower while the second and third are 20% and 10% higher, respectively. The difference diminishes with n reaching 0.3% for the 10th mode. The reason for the discrepancy in case (iii) is that the inaccurate inextensional relation of $N_{\theta\theta}$ is now enforced at the free edge, while for cases (i) and (ii) it does not appear in the boundary conditions.

3.2. Static response

Results of static response and linear stability of the panel forced by a uniform radial pressure over its entire surface are presented. The direct static analysis of the panel is developed in Appendix A. Consider a panel with $l_x = l_s = 100$ cm, $h = 1.27$ cm, bc_s:SS2 and unit radial pressure pointing towards the center of curvature. Fig. 3(a1)–(c1) plots u, v and w along s for $R = 50$ cm, and Fig. 3(a2)–(c2) plots these variables for $R = 125$ cm. v and w are evaluated at $x = l_x/2$ and u is evaluated at $x = l_x/4$ because $u(l_x/2) = 0$ (see Eq. (4a)). Instead of the expected parabolic w shape with one half wave, Fig. 3(c1) shows that w is modulated by a shape with 3 half waves producing an indentation at $s = l_s/2$. This indentation disappears when $R \geqslant 125$ cm as shown

Table 1
Arc non-dimensional resonances $\widetilde{\Omega}$

n	Clamped/clamped		Hinged/hinged		Cantilever	
	Present	De Rosa	Present	De Rosa	Present	De Rosa
1	4.3840	4.3844	2.2666	2.2667	0.2893	0.4352
2	9.6480	9.6519	6.9216	6.9233	1.7185	1.3750
3	17.912	17.922	13.972	13.978	5.2334	4.7091
4	27.492	27.524	22.801	22.819	10.897	10.515
5	39.744	39.795	33.893	33.929	18.682	18.392
6	53.354	53.473	46.720	46.798	28.547	28.335
7	69.575	69.737	61.793	61.915	40.436	40.292
8	87.121	87.448	78.570	78.800	54.334	54.266
9	107.31	107.73	97.604	97.991	70.220	70.245
10	128.68	129.11	118.28	117.82	88.087	88.211

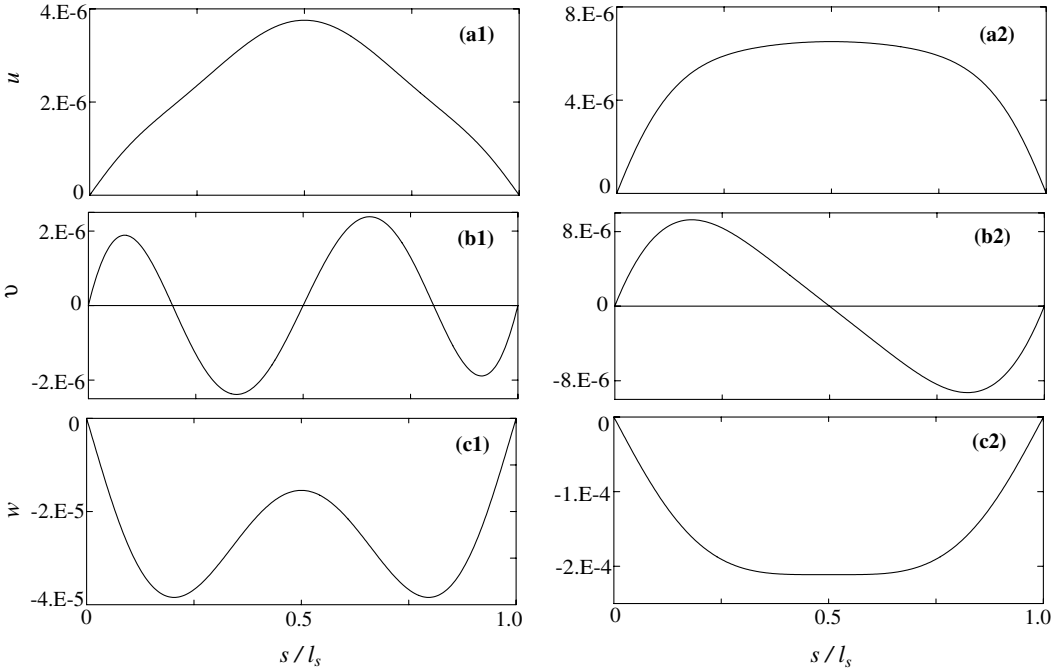

Fig. 3. Effect of R on static w shapes: bc_s:SS2, $h = 1.27$ cm. (a1)–(c1) $R = 50$ cm and (a2)–(c2) $R = 125$ cm.

in Fig. 3(c2). An explanation for the indentation is that radial pressure p_0 produces force components f_y, f_z along and normal to the chord where y,z is a Cartesian frame along these directions with origin at one of the chord's ends

$$f_y = p_0 R \int_0^{\theta_l/2} \sin(0.5\theta_l - \theta)\mathrm{d}\theta = p_0 R(1 - \cos(\theta_l/2)) = p_0 c_z$$
$$f_z = p_0 R \int_0^{\theta_l} \cos(0.5\theta_l - \theta)\mathrm{d}\theta = 2p_0 R \sin(\theta_l/2) = p_0 c_y \tag{21}$$

c_z, c_y are the panel's camber and chord. f_y is self-equilibrated meaning that for $0 \leqslant \theta \leqslant \theta_f/2$, f_y's sign is opposite to its sign for $\theta_f/2 \leqslant \theta \leqslant \theta_f$. If p_0 points towards the center, f_y's tendency is to curve the panel further while f_x's is to flatten it. The larger c_z/c_y is the larger f_y/f_x. Also, for a homogeneous material, the ratio of flexural to extensional stiffness of the plating $K_{\mathrm{flx}}/K_{\mathrm{ext}}$ is proportional to h^2. Clearly, a smaller $\sqrt{K_{\mathrm{flx}}/K_{\mathrm{ext}}} \propto h$, or a smaller R, or a larger l_s, produces the indentation. From non-dimensional analysis, a logical parameter controlling the appearance of the indentation must be proportional to $\beta = (hR)/l_s^2$.

The effect of boundary condition on the indentation is now demonstrated. Fixing h and l_s, define $\widetilde{R}$ to be the threshold of R necessary for the indentation's disappearance. For bc_s:$SS3$, Fig. 4(a1)–(c1) plots u, v and w along s for $R = 50$ cm, and Fig. 4(a2)–(c2) plots these variables for $R = 200$ cm. Note that freeing v magnifies the indentation as shown in Fig. 4(c1). Also, for bc_s:SS3 a larger $\widetilde{R}$ is needed to eliminate the indentation than for bc_s:SS2. This is expected since freeing v allows more translational elongation along s as confirmed by comparing v's magnitude in Figs. 4(b1) and 3(b1). Also, SS3 changes u's sign as evidenced by comparing Fig. 4(a1) and (a2) to Fig. 3(a1) and (a2).

To quantify the indentation and the range of parameters leading to its appearance, define the normalized indentation depth as

$$d = |(w_{\max} - w_{\min})/w_{\max}| \tag{22}$$

$w_{\max}$ is peak displacement and $w_{\min}$ is displacement at the indentation. For bc_s:SS2, Fig. 5(a) and (b) plots d against R with h as parameter for $l_x = l_s = 100$ cm and 150 cm. For smaller h or larger l_s, a larger $\widetilde{R}$ is needed

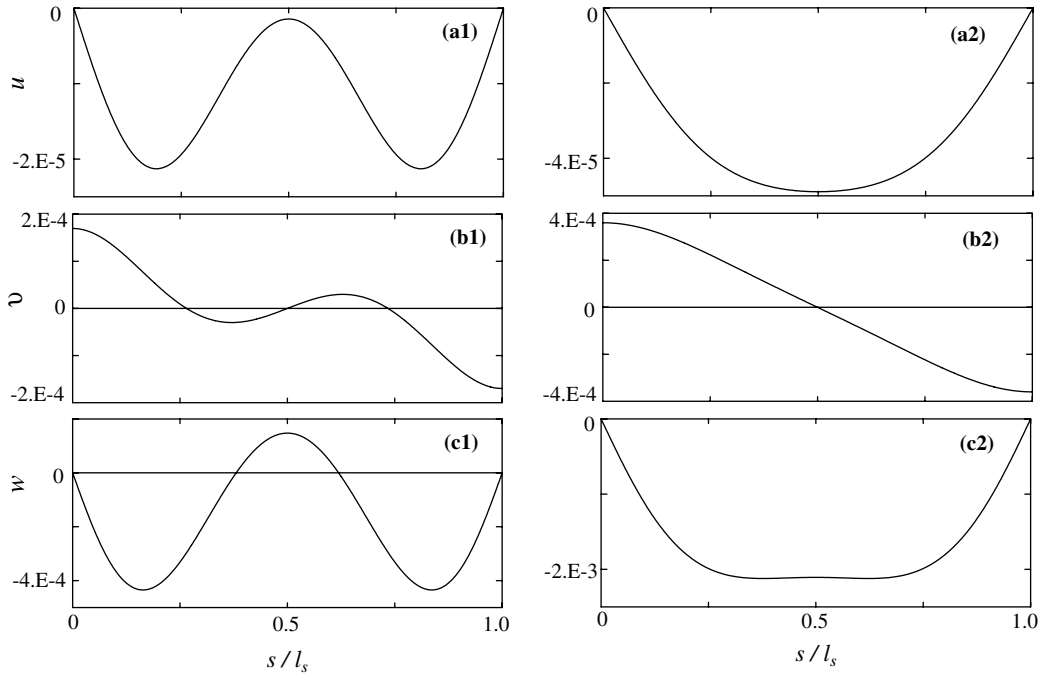

Fig. 4. Effect of R on static w shapes: bc_s:SS3, $h = 1.27$ cm. (a1)–(c1) $R = 50$ cm and (a2)–(c2) $R = 200$ cm.

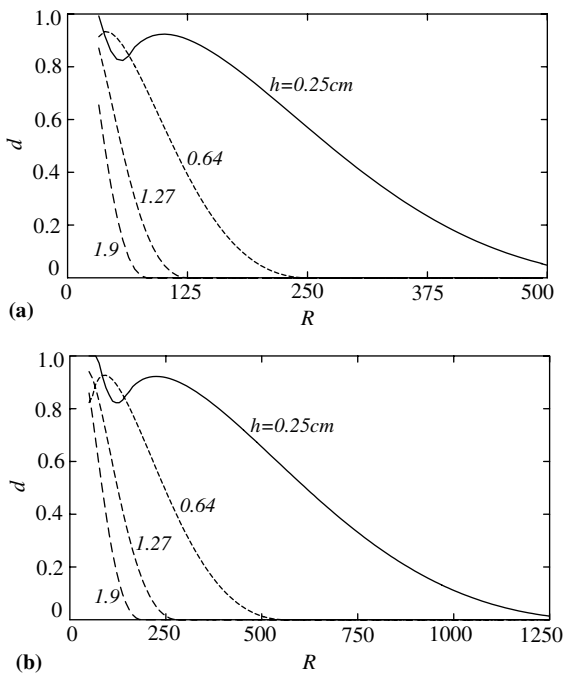

Fig. 5. Normalized indentation in static w of panel bc_s:SS2; (a) $l_s = 100$ cm, (b) $l_s = 150$ cm. (——) $h = 0.25$ cm, (-----) 0.64 cm, (- - - - -) 1.27 cm, (– – – –) 1.9 cm.

to reach $d = 0$. The same rule applies for bc_s:SS3 as shown in Fig. 6(a) and (b) which demonstrates that freeing bc_s:SS3 increases $\widetilde{R}$. What is surprising is that $\widetilde{R}$ scales quite accurately with the non-dimensional parameter

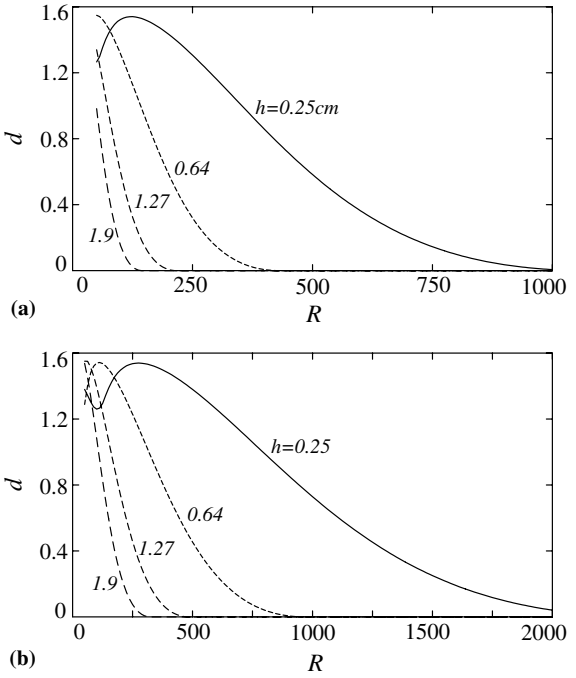

Fig. 6. Normalized indentation in static w of panel bc_s:SS3; (a) $l_s = 100$ cm, (b) $l_s = 150$ cm. (——) $h = 0.25$ cm, (-----) 0.64 cm, (- - - - -) 1.27 cm, (–––––) 1.9 cm.

$\gamma = \tilde{\beta} = \widetilde{R}h/l_s^2 \Rightarrow \widetilde{R} = \gamma l_s^2/h$. The indentation disappears when $\beta > \gamma$. For bc_s:SS2, $\gamma = 0.015$ while for bc_s:SS3, $\gamma = 0.025$. The parametric curves in Figs. 5 and 6 were reconstructed for aluminum with modulus $E = 0.67 \times 10^{12}$ dyn/cm^2 revealing that for some fixed h, the shape of the d curves and the corresponding $\widetilde{R}$'s are independent of modulus and vary only with geometry. Obviously, magnitude of any dependent variable is proportional to E yet its spatial distribution is independent of E provided the material is homogeneous.

In contrast to the finite panel, the arc's static deformation excludes the indentation independent of the parameter space. This suggests that a condition for its appearance is a state of bi-axial stress.

Results from the direct static solution in Appendix A are validated by a modal solution to the static problem in the following way. In Eqs. (11) and (12) set $\ddot{a}(t) = 0$, yielding the static displacement vector in terms of the eigenfunctions

$$\mathbf{G}_{\mathrm{G}} = \sum_n \sum_m a_{nm} \mathbf{\Phi}_{nm}(\theta) \mathbf{\Psi}_m(x), \quad a_{nm} = -N_{fn,m}/(\omega_{nm}^2 N_{nn,m}) \tag{23}$$

Comparing magnitude and shape of displacements from the two solutions in Fig. 7(a1)–(c1) and Fig. 7(a2)–(c2) confirms that results from the two methods coincide.

3.3. Static stability

The stability analysis developed in Appendix B that excludes initial displacement $w_0(x, \theta)$ is applied to an arc. Due to the uniform loading and bilateral symmetry about $\theta_l/2$ and $l_x/2$, only modes with odd n and m are included. Since p_{crt} increases with E and flexural stiffness h^3, and diminishes with R and l_s, non-dimensional analysis determines a normalization pressure per unit width of the arc proportional to $\pi E h^3/(R l_s) = p_0$. Indeed, for the arc a plot of p_{crt}/p_0 versus wave number n of the buckling mode (Fig. 8(a)) is invariant for all parameters. The lowest $p_{\mathrm{crt}} \equiv p_{\min}$ always occurs at $n = 3$. For $n \geqslant 3$, the arc's p_{crt} can now be approximated by

$$p_{\mathrm{crt}}/(\pi E h^3/(R l_s)) \approx 7.19 \times 10^{-3} n^2 \tag{24}$$

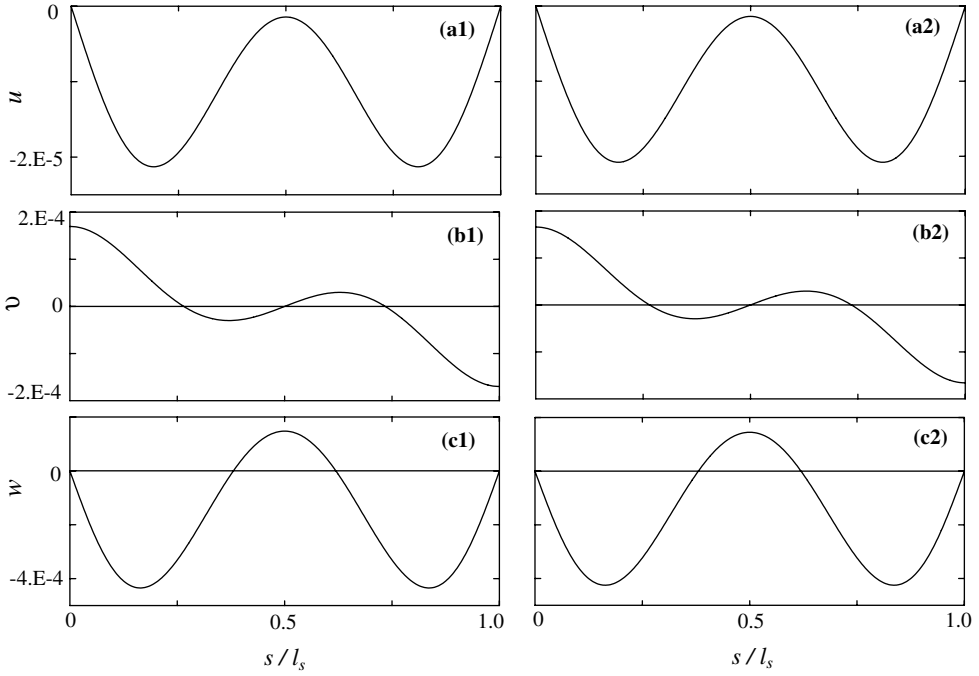

Fig. 7. Comparison of static w from direct and modal solutions bc_s:SS3; $h = 1.27$ cm, $R = 50$ cm. (a1)–(c1) direct, (a2)–(c2) modal.

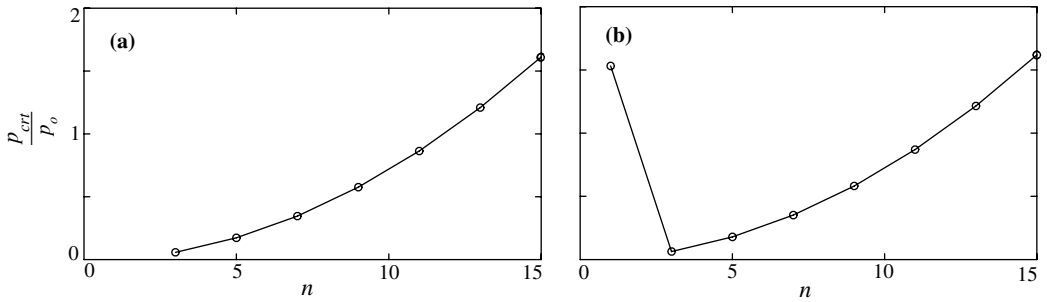

Fig. 8. Arc critical pressure p_{crt}/p_0, $p_0 = \pi Eh^3/(Rl_s)$. (a) $Rh/l_s^2 = 0.014$ and (b) $Rh/l_s^2 = 0.022$.

p_{crt} with $n = 1$ appears only when $\beta = Rh/l_s^2 > \gamma$ (see Fig. 8(b)), where γ is the parameter controlling the indentation's appearance in static deformation, and is much higher than $p_{\min}$.

Fig. 9 plots p_{crt}/p_0 versus n with m as parameter for the finite panel. The normalizing p_0 is kept the same as the arc's since pressure per unit arc width still applies because of the uniform pressure distribution. In Fig. 9(a) and (b) both R and h vary keeping $R \times h$ and l_s constants and in both cases $\beta = 0.006$. Note that the corresponding m lines in both figures coincide. At $m = 1$, $p_{\min}$ occurs at $n = 3$ while for $m = 5$ and 7, $p_{\min}$ shifts to $n = 7$. In Fig. 9(c) and (d), R and l_s vary while h is held constant. The m-lines now differ from those in Fig. 9(a) and (b). Unlike the arc's case, the panel's p_{crt} is not controlled by a single parameter.

To understand p_{crt}'s dependence on R, h and l_s, Fig. 10(a) plots p_{crt}/p_0 versus R/h_0 for $h_0 = 1.27$ cm and $l_s = l_x = 100$ cm. A second ordinate on top of the figure is for Rh/l_s^2. In the interval $25 < R/h_0 < 100$, p_{crt}/p_0 drops sharply then flattens reaching an asymptote of $p_{\mathrm{crt}}/p_0 \approx 0.075$ for $R/h_0 > 250$. A similar behavior applies to p_{crt}/p_0 versus h/R_0 for $R_0 = 50$ cm and $l_s = l_x = 100$ cm as shown in Fig. 10(b). Fig. 10(c) plots p_{crt}/p_0 versus $(l_s/R_0)^2$ keeping $l_x = l_s$ for $R_0 = 100$ cm and $h_0 = 1.27$ cm. There also, as l_s increases it approaches $p_{\mathrm{crt}}/p_0 \approx 0.075$. Two observations can be made from Fig. 10(a)–(c)

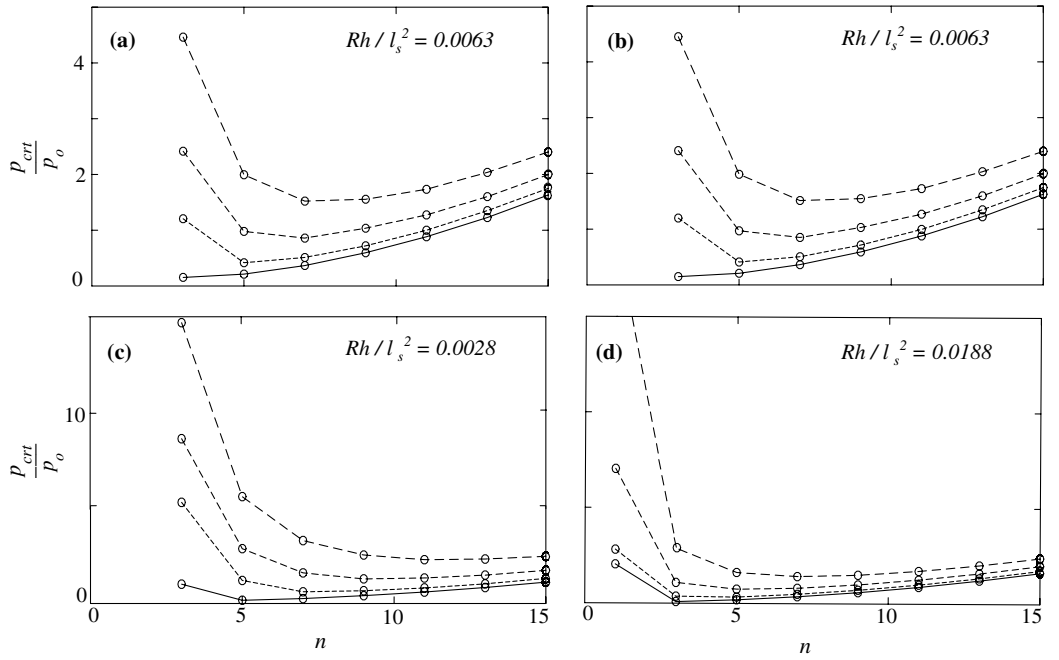

Fig. 9. Panel critical pressure p_{crt}/p_0 vs n, $p_0 = \pi Eh^3/(Rl_s)$. (——) $m = 1$, (- - - - -) $m = 3$, (- - - - -) $m = 5$, (– – – –) $m = 7$. (a) $R/h = 40$, $l_s/R = 2$; (b) $R/h = 160$, $l_s/R = 1$; (c) $R/h = 40$, $l_s/R = 3$ and (d) $R/h = 120$, $l_s/R = 2/3$.

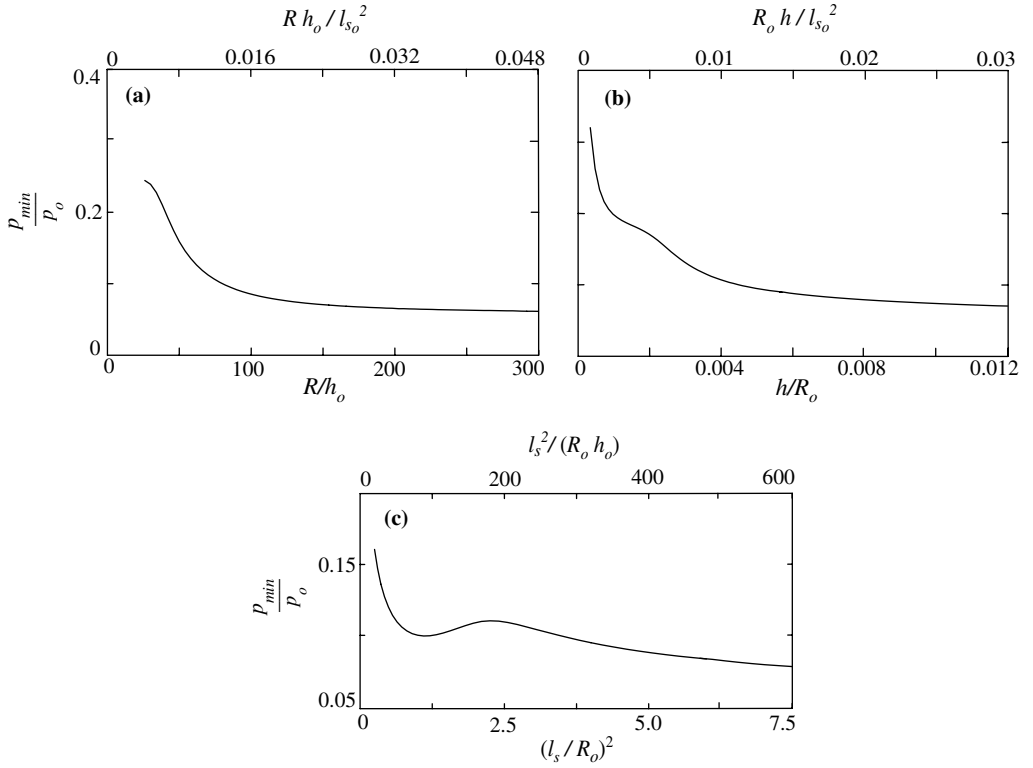

Fig. 10. Effect of R, h and l_s on minimum critical pressure p_{min}/p_0, $p_0 = \pi Eh^3/(Rl_s)$. (a) $h_0 = 1.27$ cm, $l_{s0} = l_{x0} = 100$ cm; (b) $R_0 = 50$ cm, $l_{s0} = l_{x0} = 100$ cm; (c) $R_0 = 100$ cm, $h_0 = 1.27$ cm.

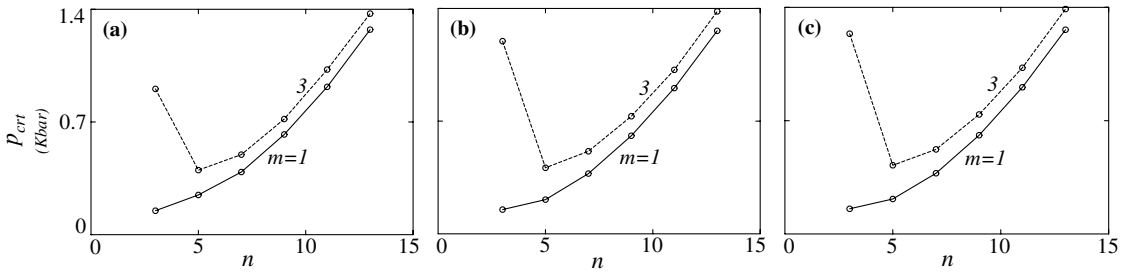

Fig. 11. Effect of pre-buckling w_0 on p_{crt}. $R = 50$ cm, $l_x = l_y = 100$ cm, $h = 1.27$ cm; (——) $m = 1$, (-----) $m = 3$. (a) Modal, including w_0; (b) modal, excluding w_0; (c) direct, excluding w_0.

(1) The approach of p_{crt} to the parametric form $h^3/(Rl_s)$ starts when $Rh/l_s^2 \equiv \beta > 0.015$ coinciding with the indentation's critical β in static deformation.
(2) The three asymptotic values $p_{crt}/p_0 \approx 0.075$ in Fig. 10(a)–(c) are close to the arc's approximation for p_{crt} in (24) which is $p_{crt}/p_0 \approx 0.065$. This means that as R, h and l_s increase, the panel's p_{crt} approaches the arc's following the form $h^3/(Rl_s)$.

For a panel with bc_s:SS2, Fig. 11(a) and (b) plots p_{crt} versus n with m as parameter adopting the analysis in Appendix B with and without the effect of pre-buckling w_0. For $m = 1$, w_0 reduces the minimum p_{crt} corresponding to $n = 3$ by 3%, and raises p_{crt} for all $n \geqslant 5$. For $n = 5$, the rise in p_{crt} is 15% then diminishes smoothly with n as evidenced when comparing the $m = 1$ line in Fig. 11(a) to that in Fig. 11(b). Comparing the p_{crt} lines in Fig. 11(b) from the modal solution to those in Fig. 11(c) from a direct solution of the stability problem confirms that modal and direct solutions yield identical results validating the analysis.

The effect on p_{crt} of initial imperfection is qualitatively similar to the effect of pre-buckling deformation. Except for magnitude of w_0 and its shape, the analysis developed in Appendix B applies to static stability with initial imperfection. The effect of imperfection is omitted as it is beyond the scope of the present study.

The effect of w_0 on the radial buckling mode w_{crt} is demonstrated by comparing corresponding modes for $n = 3$ and $n = 5$, including and excluding w_0. Fig. 12(a1) and (b1) plot these modes including w_0 and Fig. 12(a2) and (b2) plot the same modes excluding w_0. Mode $n = 3$ is not affected by w_0 while mode $n = 5$ differs appreciably near the center, consistent with bc_s:SS3's effect on p_{crt}. From the results above it appears that the lowest p_{crt} and w_{crt} are insensitive to w_0.

3.4. Transient response

The panel is forced by a uniformly distributed impulsive pressure of unit intensity following a trapezoidal time dependence with 3 μs rise time, 10 μs fall time and 287 μs plateau. Two boundary conditions are considered

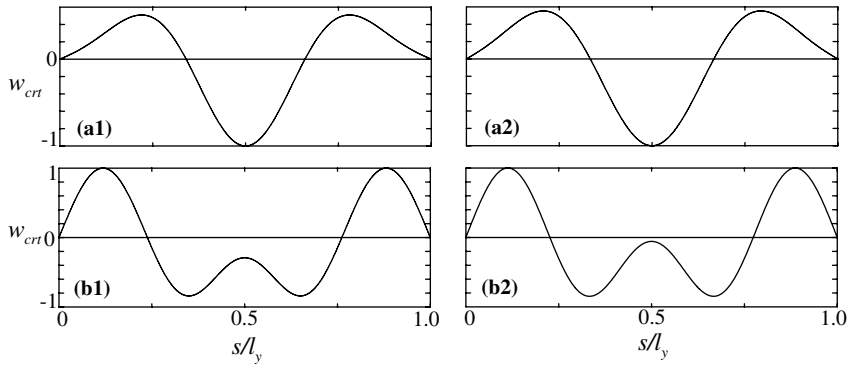

Fig. 12. Effect of pre-buckling w_0 on buckling mode at $x = l_x/2$. w_{crt} including w_0, (a1) $n = 3$, (b1) $n = 5$; w_{crt} excluding w_0, (a2) $n = 3$, (b2) $n = 5$.

along the straight edges: bc_s:SS2 and bc_s:SS3 as described by 20(b,c). In all cases, $l_x = l_s = 100$ cm and θ. Two values of R are considered 100 cm and 150 cm that lie on different sides of the threshold $\widetilde{R}$ for appearance of the indentation in the static deformation shape (see Figs. 5 and 6(a)).

Plots of the panel's frequency spectra versus mode number with axial wave number m as parameter are shown in Fig. 13(b) for bc_s:SS3 and $R = 150$ cm, and in Fig. 13(b) for bc_s:SS3 and $\mathbf{T}_{\mathrm{G}m}$. In spite of the different R and boundary conditions, the two spectra almost coincide. This is the first indication that static and dynamic parameters are unrelated.

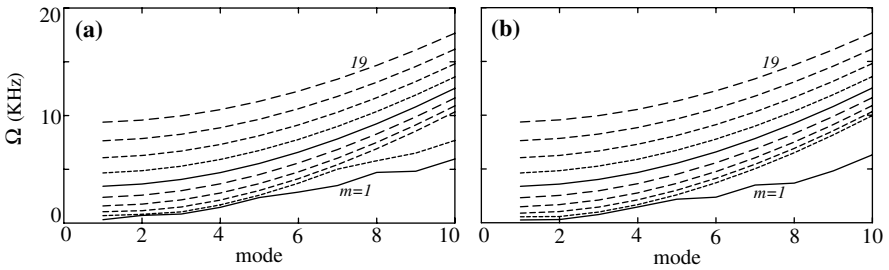

Fig. 13. Frequency spectra; $h = 1.27$ cm, $l_x = l_s = 100$ cm. (a) bc_s:SS2, $R = 100$ cm, (b) bc_s:SS3, $R = 150$ cm.

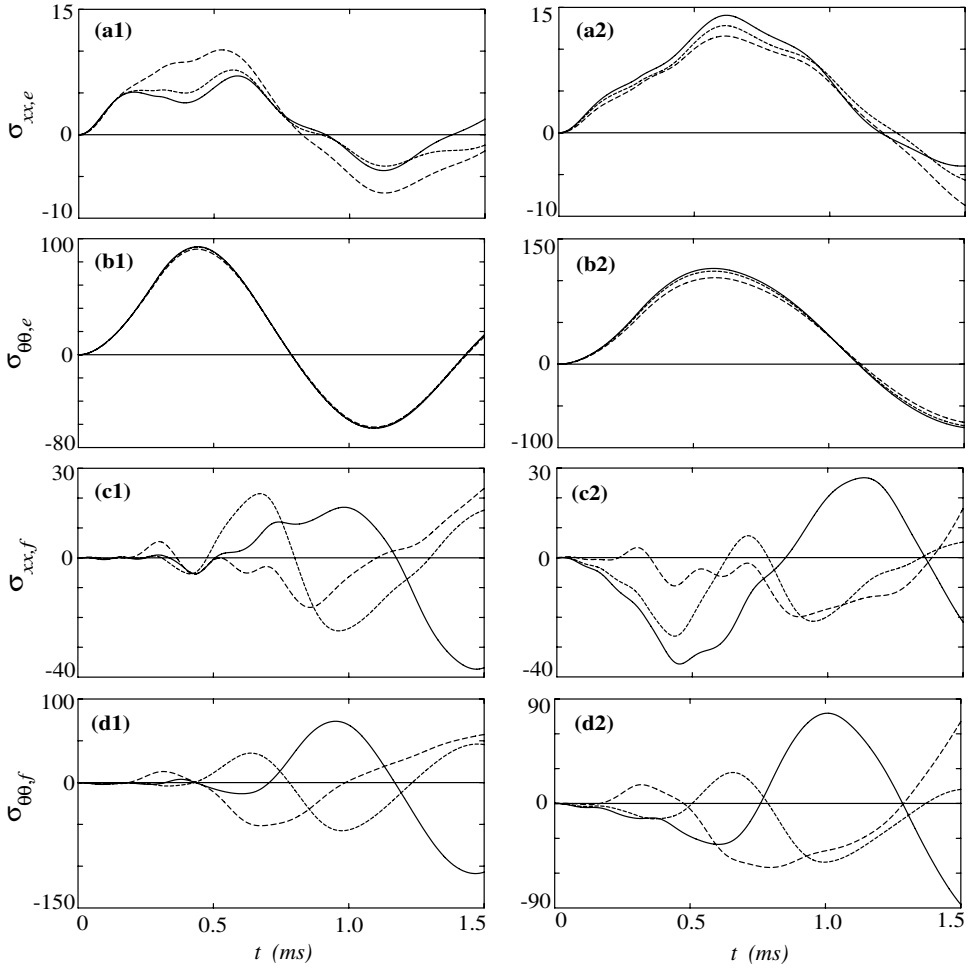

Fig. 14. Stress histories; bc_s:SS2, h=1.27 cm, $l_x = l_s = 100$ cm. (——) $s = 0.5l_s$, (- - - - -) $s = 0.63l_s$, (- - - - -) $s = 0.75l_s$. (a1)–(d1) $R = 100$ cm; (a2)–(d2) $R = 150$ cm.

For bc_s:SS2, Fig. 14(a1)–(d1) plot stress histories for $R = 100$ cm and Fig. 14(a2)–(d2) plot these histories for $R = 150$ cm, at three different locations along s. In these figures, $\sigma_{xx,e}$, $\sigma_{\theta\theta,e}$ are axial and circumferential extensional stresses, while $\sigma_{xx,f}$, $\sigma_{\theta\theta,f}$ are axial and circumferential flexural stresses. Note that peak stress of corresponding stress components reach approximately the same magnitude independent of R. In Fig. 14(b1) and (b2), $\sigma_{\theta\theta,e}$ at the different s stations almost coincide meaning that $\sigma_{\theta\theta,e}$ is approximately constant along s. In fact, peak $\sigma_{\theta\theta,e}$ is slightly higher than the static value $\sigma_{\theta\theta,e\ s} \approx p_0 R/h = 80$.

For bc_s:SS3, Fig. 15(a1)–(d1) plot stress histories $R = 100$ cm, and Fig. 15(a2)–(d2) plot these histories for $R = 150$ cm. Once more, peak stress is independent of R. With the exception of $\sigma_{xx,e}$, peak stresses in Fig. 14 are approximately the same as corresponding peak stresses in Fig. 15. The same observation does not apply to Fig. 16, which plots distribution of static stresses along s for the two boundary conditions. For bc_s:SS2, $\sigma_{xx,es}$, $\sigma_{xx,fs}$, $\sigma_{\theta\theta,fs}$ are one order of magnitude lower than the corresponding stresses for bc_s:SS3. This is a stronger indication that static and dynamic responses are unrelated.

Keeping the same forcing pulse as the panel's, Fig. 17(a1) and (b1) plots stress histories of the ring with $R = 100$ cm and bc_s:SS2, while Fig. 17(a2) and (b2) plots these histories for bc_s:SS3. Comparing Fig. 17(a1) and (b1) of the ring to Fig. 14(b1) and (d1) of the panel shows that the corresponding $\sigma_{\theta\theta,e}$ and $\sigma_{\theta\theta,f}$ are comparable in magnitude and shape. This also applies to $\sigma_{\theta\theta,f}$ in Fig. 17(b2) and Fig. 15(d1). However for bc_s:SS3, $\sigma_{\theta\theta,e}$ of the ring is much smaller than that of the panel (compare Fig. 17(a2) to Fig. 15(b1)). The reason is that

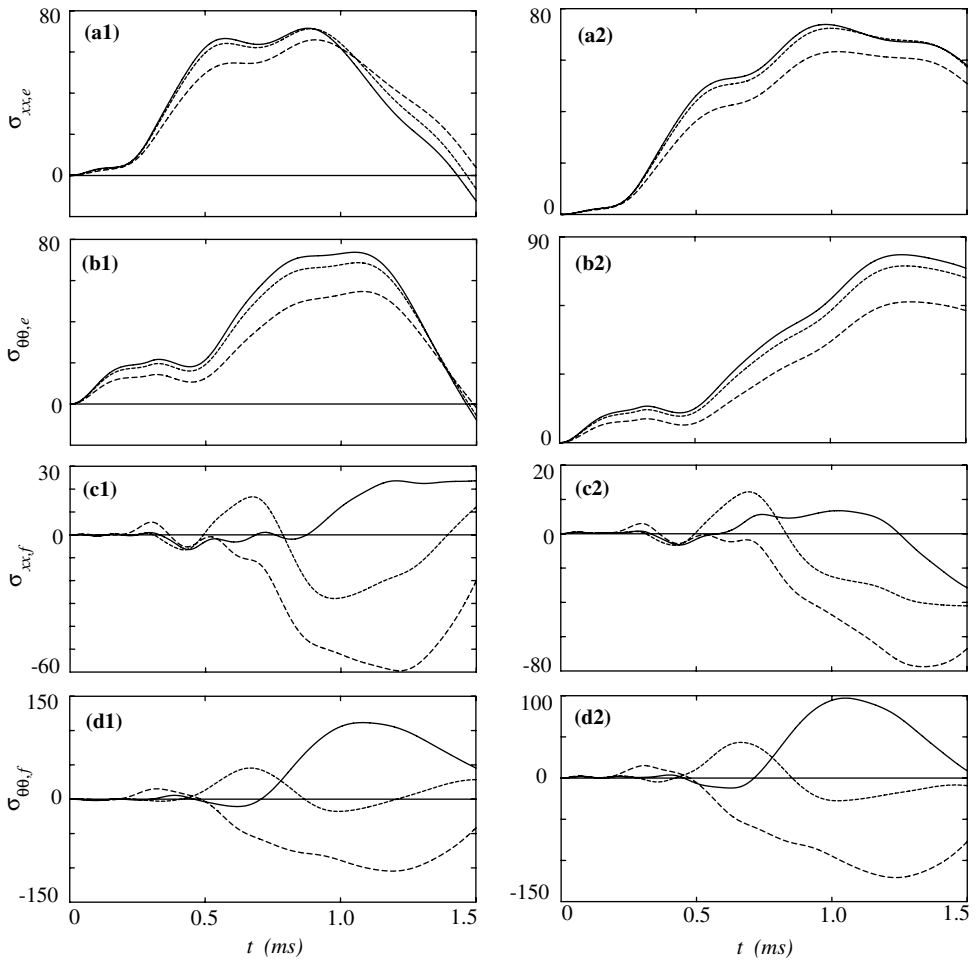

Fig. 15. Stress histories; bc_s:SS3, $h = 1.27$ cm, $l_x = l_s = 100$ cm. (——) $s = 0.5l_s$, (- - - - -) $s = 0.63l_s$, (- - - - -) $s = 0.75l_s$. (a1)–(d1) $R = 100$ cm; (a2)–(d2) $R = 150$ cm.

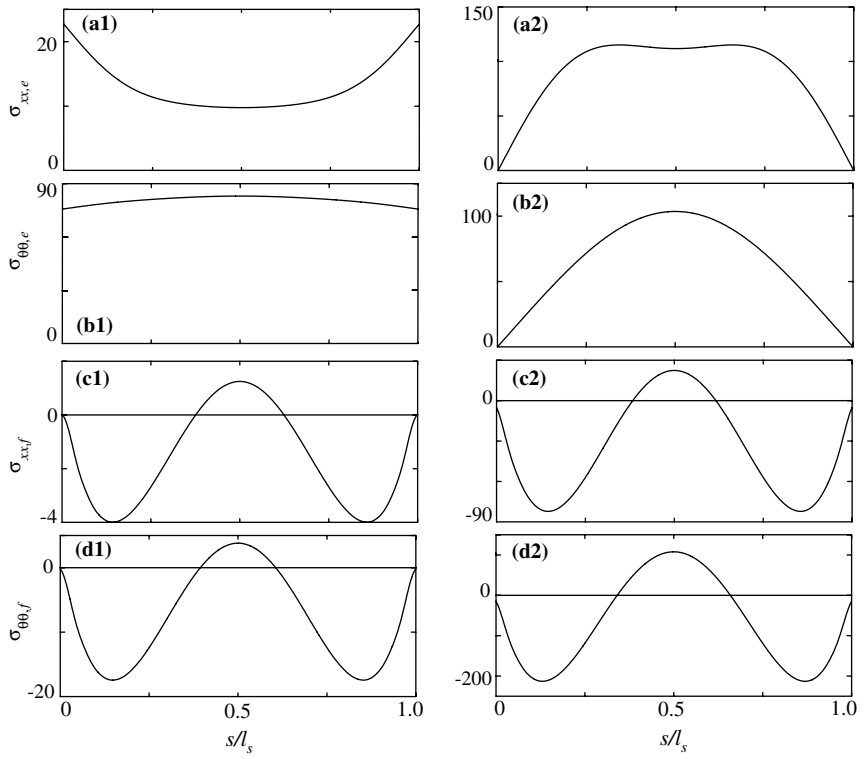

Fig. 16. Distribution of static stress along s; $h = 1.27$, $R = 100$ cm, $l_s = l_x = 100$ cm. (a1)–(d1) bc_s:SS2, (a2)–(d2) bc_s:SS3.

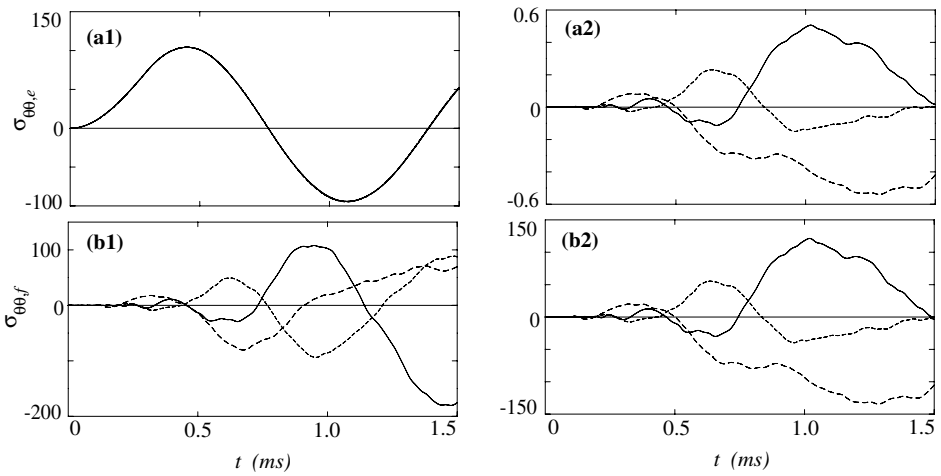

Fig. 17. Stress histories of ring; $R = 100$ cm, $h = 1.27$ cm, $l_s = 100$ cm. (——) $s = 0.5l_s$, (-----) $s = 0.63l_s$, (- - - - -) $s = 0.75l_s$. (a1), (b1) bc_s:SS2; (a2), (b2) bc_s:SS3.

for bc_s:SS3, $\sigma_{\theta\theta,e}$ vanishes at the ends, keeping magnitude small throughout the arc. For the panel, coupling of axial and circumferential variables increases resistance to motions along θ, explaining the panel's higher $\sigma_{\theta\theta,e}$.

Fig. 18 plots snap-shots of the panel's deformed shapes along s at constant time intervals for the two boundary conditions. At 0.4 ms, the instantaneous mode in Fig. 18(b1) shows the start of two inflexions symmetric about $s = l_s/2$. At 0.6 ms, these inflexions magnify and at 0.8 ms the mode acquires 5 half waves. At 0.6 ms, the mode with 3 half waves in Fig. 18(c2) varies smoothly along s, and this shape is maintained at

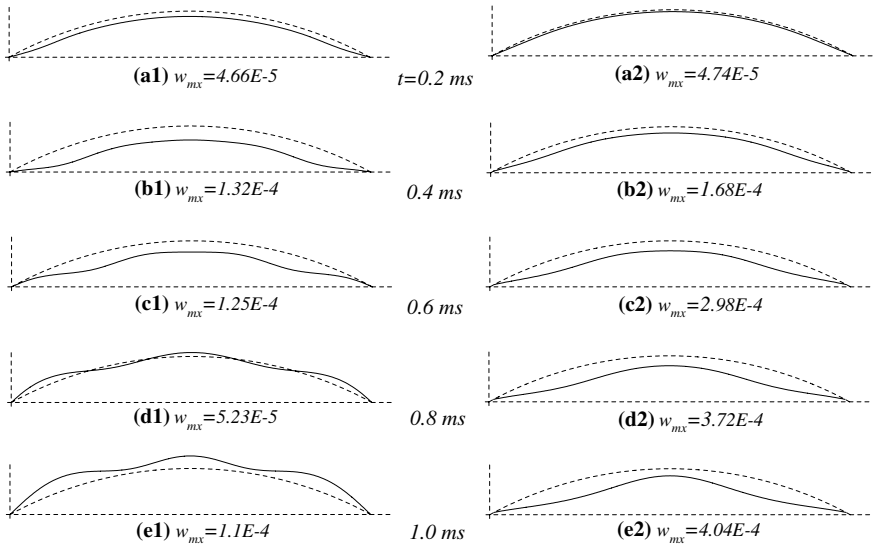

Fig. 18. Time snap-shots of deformed shape at $x = l_x/2$. $h = 1.27$, $R = 100$ cm, $l_s = l_x = 100$ cm. (a1)–(e1) bc_s:SS2, (a2)–(e2) bc_s:SS3.

0.8 ms and 1 ms. Comparing snapshots for bc_s:SS2 in Fig. 18(a1)–(e1) to those for bc_s:SS3 in Fig. 18(a2)–(e2) reveals that the higher wave number response mode of SS2 is balanced by the larger amplitude of SS3 thus keeping peak stresses for both boundary conditions approximately the same.

4. Conclusion

For static response, noteworthy results are:

(1) An indentation in the static shape forms when the non-dimensional parameter $\beta \equiv (hR)/l_s^2 \leqslant \gamma$, where γ is a constant that depends only on boundary conditions along the straight edge of the panel.
(2) For a homogeneous material, γ is independent of material properties. For bc_s:SS2, $\gamma = 0.015$ while for bc_s:SS3, $\gamma = 0.025$.
(3) Panel stiffness is more sensitive to inplane boundary conditions (SS2) than it is to flexural constraints (SS3) consistent with the result of Kistler and Waas (1999).

For static stability, noteworthy results are:

A. For the arc,
  (1) A normalization parameter $p_0 = \pi Eh^3/(Rl_s)$ yields a p_{crt}/p_0 invariant with geometry and properties, that depends only on wave number n of the buckling mode.
  (2) The lowest $p_{\text{crt}} \equiv p_{\min}$ always occurs at $n = 3$. For $n \geqslant 3$, the arc's p_{crt} can now be approximated by $p_{\text{crt}}/(\pi Eh^3/(Rl_s)) \approx 7.19 \times 10^{-3} n^2$.
  (3) p_{crt}'s mode with $n = 1$ appears only when $\beta = Rh/l_s^2 > \gamma$ where γ is the parameter controlling the indentation's appearance in static deformation. In this case $p_{\text{crt}}\ (n = 1) \gg p_{\min}$.
B. For the finite panel,
  (4) For $m = 1$, $p_{\min}$ occurs at $n = 3$. As m increases, $p_{\min}$ shifts to higher n's.
  (5) Keeping the same normalizing parameter p_0 as the arc's, p_{crt}/p_0 drops sharply with R in the interval $25 < R/h_0 < 100$, then flattens reaching an asymptote of $p_{\text{crt}}/p_0 \approx 0.075$ for $R/h_0 > 250$.
  (6) A similar behavior applies to how p_{crt}/p_0 varies with h.
  (7) The approach of p_{crt} to the parametric form $h^3/(Rl_s)$ starts when $Rh/l_s^2 \equiv \beta > 0.015$, a value coinciding with the indentation's critical β in static deformation.

(8) The three asymptotic values of p_{crt}/p_0 with R, h and l_s are close to the arc's approximation for $p_{crt}/p_0 \approx 0.065$. This means that as R, h and l_s increase, the panel's p_{crt} asymptotically follows the arc's dependence on $h^3/(Rl_s)$.
(9) The effect on p_{crt} of pre-buckling w_0 is to lower p_{min} ($n = 3$) slightly. For $n = 5$, w_0 raises p_{crt} by an appreciable amount. This rise diminishes smoothly as n increases.

For transient response, noteworthy results are:

(1) Frequency spectra are insensitive to geometry and boundary conditions.
(2) Changing R below and above the critical $\widetilde{R}$ controlling the appearance of the indentation in the static mode has no effect on peak dynamic stresses.
(3) With the exception of $\sigma_{xx,f}$, peak dynamic stresses due to impulse of short duration are insensitive to extensional boundary constraint.
(4) With the exception of $\sigma_{\theta\theta,e}$, peak dynamic stresses due to an impulse of short duration are substantially different from their static counterparts, confirming that static and dynamic responses are unrelated.
(5) The higher wave number response mode of SS2 is balanced by the larger amplitude of SS3, thus keeping peak stresses for both boundary conditions approximately the same.
(6) For SS2, corresponding $\sigma_{\theta\theta,f}$ and $\sigma_{\theta\theta,e}$ of ring and panel are similar in magnitude and shape, while for SS3 only $\sigma_{\theta\theta,f}$ are similar.

Appendix A. Direct static solution

Eliminating time dependence from (1) to (4) of the text, setting $\omega = 0$ in (5), and following the same steps that led to the global transfer matrix (8) yields the global inhomogeneous block tri-diagonal equations for each axial wave number m

$$\mathbf{T}^{(s)}_{Gm}\mathbf{S}^{(s)}_{Gm} = \mathbf{P}^{(s)}_{m} \tag{A.1}$$

Superscript (s) refers to "static" noting that $\mathbf{T}^{(s)}_{Gm}$ in (A.1) is the equivalent of $\mathbf{T}_{Gm}$ in (8) in the limit when $\omega = 0$. The total static state vector $\mathbf{S}^{(s)}_{G}$ is the sum of all $\mathbf{S}^{(s)}_{Gm}$

$$\mathbf{S}^{(s)}_{G} = \sum_m \mathbf{S}^{(s)}_{Gm} \tag{A.2}$$

What remains is to establish how the right hand vector $\mathbf{P}^{(s)}_{m}$ is related to the external uniform radial pressure p_0. The external pressure can be modeled in one of two ways:

(1) Equivalent radial force $q_{ej,m}$ counteracted by the shear resultant $Q_{\theta j,m}$ at the interface of segments jth and $(j+1)$th where $q_{ej,m} = p_0 a(\theta_{j+1} - \theta_j)(4/m\pi)$. The factor $(4/m\pi)$ comes from the elimination of axial dependence by orthogonality. In this way the components of

$$\mathbf{P}^{(s)}_{m} = \{\mathbf{0}, \mathbf{p}_{1m}, \mathbf{0}, \mathbf{p}_{2m}, \ldots, \mathbf{0}, \mathbf{p}_{jm}, \ldots, \mathbf{0}, \mathbf{p}_{(m_s-2)m}, \mathbf{0}, \mathbf{0}, \mathbf{0}, \mathbf{0}\}^{\mathrm{T}} \quad \text{are} \quad \mathbf{p}_{jm} = \{0, 0, q_{ejm}, 0\}^{\mathrm{T}}.$$

(2) Re-defining the transfer matrix to include the inhomogeneous solution for uniform radial pressure.

The procedure in method (2) is outlined in what follows. Noting that the axial solution decouples for each m, then for a uniform radial pressure p_0 the inhomogeneous static displacement of the jth segment becomes

$$\begin{aligned}
u_{sj}(\theta, x) &= \sum_m \left[\sum_{k=1}^{8} u_{kjm} c_{skjm} e^{\alpha_{kjm}\theta} + c_{ujm}\right] C_m(x) \\
v_{sj}(\theta, x) &= \sum_m \sum_{k=1}^{8} v_{kjm} c_{skjm} e^{\alpha_{kjm}\theta} S_m(x) \\
w_{sj}(\theta, x) &= \sum_m \left[\sum_{k=1}^{8} w_{kjm} c_{skjm} e^{\alpha_{kjm}\theta} + c_{wjm}\right] S_m(x)
\end{aligned} \tag{A.3}$$

c_{ujm}, c_{wjm} are constants. Substituting (A.3) in the static equivalent of (1a)–(1c), eliminating the x dependence by enforcing orthogonality of $S_m(x)$, $C_m(x)$, then equating constant terms to zero yields the inhomogeneous solution

$$\begin{aligned} c_{wjm} &= 4p_0(N_0(1-\nu^2)/R^2 + M_0 k_{xm}^4)^{-1}/(m\pi) \\ c_{ujm} &= -\nu c_{wjm}/(k_{xm}R) \end{aligned} \tag{A.4}$$

The transfer equation (8) that includes the inhomogeneous solution becomes

$$\mathbf{S}_{jm}(\theta_{j+1}) = \mathbf{T}_{(j,j+1)m}\mathbf{S}_{jm}(\theta_j) + [\mathbf{S}_{0jm}(\theta_{j+1}) - \mathbf{T}_{(j,j+1)m}\mathbf{S}_{0jm}(\theta_j)] \tag{A.5}$$

On the right hand side of (A.5), the first term is the homogeneous part equivalent to Eq. (8), and the square bracketed term is the inhomogeneous part forming the right hand vectors $\mathbf{P}_m^{(s)}$

$$\begin{aligned} \mathbf{P}_m^{(s)} &= \{\mathbf{0}, \mathbf{p}_{1m}, \mathbf{q}_{1m}, \mathbf{p}_{2m}, \ldots, \mathbf{q}_{(j-1)m}, \mathbf{p}_{jm}, \ldots, \mathbf{q}_{(m_s-2)m}, \mathbf{p}_{(m_s-1)m}, \mathbf{q}_{(m_s-1)m}, \mathbf{0}\}^{\mathrm{T}} \\ \mathbf{p}_{jm} &= \mathbf{f}_{0jm}(\theta_{j+1}) - (\mathbf{t}_{11,jm}\mathbf{f}_{0jm}(\theta_j) + \mathbf{t}_{12,jm}\mathbf{g}_{0jm}(\theta_j)) \\ \mathbf{q}_{jm} &= \mathbf{g}_{0jm}(\theta_{j+1}) - (\mathbf{t}_{21,jm}\mathbf{f}_{0jm}(\theta_j) + t_{22,jm}\mathbf{g}_{0jm}(\theta_j)) \end{aligned} \tag{A.6}$$

In (A.6), $\mathbf{t}$ are the transfer sub-matrices defined in (9). Components of $\mathbf{f}_{0jm} = \{f_{01}, f_{02}, f_{03}, f_{04}\}_{jm}^{\mathrm{T}}$ and $\mathbf{g}_{0jm} = \{g_{01}, g_{02}, g_{03}, g_{04}\}_{jm}^{\mathrm{T}}$ vanish except for

$$\begin{aligned} (f_{02})_{jm} &= -N_0(\nu k_{xm} c_{ujm} + c_{wjm}/R) \\ (g_{01})_{jm} &= c_{ujm}, \quad (g_{03})_{jm} = c_{wjm} \end{aligned} \tag{A.7}$$

If the panel is inhomogeneous along s, then N_0 varies with j also.

Appendix B. Linear static stability

When including the nonlinear moments from inplane stress resultants, the third static equation in (1a) becomes

$$D_{s31}(u) + D_{s32}(v) + D_{s33}(w) + N_{\theta\theta}\partial_{\theta\theta}w/R^2 = 0 \tag{B.1a}$$

Linearizing the third term in (B.1a) yields

$$\begin{aligned} &N_{\theta\theta}\partial_{\theta\theta}w \approx N_{\theta\theta 0}(\partial_{\theta\theta}w + N_{\theta\theta}\partial_{\theta\theta}w_0) \\ &\quad \Rightarrow \; D_{s31}(u) + D_{s32}(v) + D_{s33}(w) + N_{\theta\theta 0}\partial_{\theta\theta}w/R^2 + N_{\theta\theta}N_{\theta\theta 0}\partial_{\theta\theta}w_0/R^2 = 0 \end{aligned} \tag{B.1b}$$

$N_{\theta\theta 0}$ is applied uniform stress resultant and $w_0(x,\theta)$ is pre-buckling static radial displacement from unit pressure. Expanding the added terms in (B.1b) produces the linear static stability equations

$$\begin{aligned} &D_{s11}(u) + D_{s12}(v) + D_{s13}(w) = 0 \\ &D_{s21}(u) + D_{s22}(v) + D_{s23}(w) = 0 \\ &(D_{s31} + D_{b31})(u) + (D_{s32} + D_{b32})(v) + (D_{s33} + D_{b33})(w) = 0 \end{aligned} \tag{B.1c}$$

$$\begin{aligned} D_{s11} &= N_0(\partial_{xx} + (1-\nu)\partial_{\theta\theta}/2R^2) \\ D_{s12} &= D_{s21} = N_0(1+\nu)\partial_{x\theta}/2R \\ D_{s13} &= D_{s31} = -N_0\nu\partial_x/R \\ D_{s23} &= D_{s32} = -N_0\partial_\theta/R^2 + M_0\partial_\theta(\partial_{\theta\theta}/R^2 + (2-\nu)\partial_{xx})/R^2 \\ D_{s33} &= M_0\nabla^4 + N_0/R^2 \end{aligned} \tag{B.1d}$$

$$\begin{aligned} D_{b31} &= \varepsilon_b(N_0/a^2)^2\partial_{\theta\theta}w_0(x,\theta)\nu R\partial_x \\ D_{b32} &= \varepsilon_b(N_0/a^2)^2\partial_{\theta\theta}w_0(x,\theta)\partial_\theta \\ D_{b33} &= \varepsilon_b(N_0/a^2)\partial_{\theta\theta} - \varepsilon_b(N_0/a^2)^2\partial_{\theta\theta}w_0(x,\theta) \\ \varepsilon_b &= N_{\theta\theta 0}/N_0 \end{aligned} \tag{B.1e}$$

In (B.1c), D_{sij}, $i,j=1,2,3$ are the same operators as D_{ij}, $i,j=1,2,3$ in (1a) but with vanishing time dependence, and D_{b31}, D_{b32}, D_{b33} account for geometric stiffness. In the stability problem, the inhomogeneous terms in (B.1e) resemble the terms accounting for initial imperfection. N_{xx0} does not appear because of the traction-free boundary conditions bc_x:SS1 at $x=0$, l_x defined by Eq. (20a).

The first part of the stability analysis excludes the effect of $w_0(x,\theta)$ and only the $N_{\theta\theta 0}$ term $\varepsilon_b(N_0/a^2)\partial_{\theta\theta}$ in D_{b33} is kept. The analysis repeats the steps in Section 1 of the text. The basic equations are outlined here for completeness. Displacement is expanded as in (4a)–(4c)

$$u(x,\theta)=\sum_{m=1}\sum_{k=1}^{8}u_{km}\mathrm{e}^{\alpha_{km}\theta}C_m(x) \tag{B.2a}$$

$$v(x,\theta)=\sum_{m=1}\sum_{k=1}^{8}v_{km}\mathrm{e}^{\alpha_{km}\theta}S_m(x) \tag{B.2b}$$

$$w(x,\theta)=\sum_{m=1}\sum_{k=1}^{8}w_{km}\mathrm{e}^{\alpha_{km}\theta}S_m(x) \tag{B.2c}$$

$S_m(x)$, $C_m(x)$ are defined in (4c). Substituting (B.2a)–(B.2c) in (B.1a) noting that $S_m(x)$, $C_m(x)$ are orthogonal yields an 8th order polynomial in the complex exponents α_{km} for each m

$$\sum_{k=0}^{4}c_{km}\alpha_{km}^{2k}=0 \tag{B.3}$$

Coefficients c_{km} are similar to those in (5) with $\omega=0$ and with the added terms multiplying ε_b. Following the same steps that led to Eqs. (6)–(9) of the text yields the implicit eigenvalue problem (9) and the eigenset $\{\mathbf{G}_{sG},\varepsilon_b\}_{nm}$ that determines the critical pressure and buckling mode with (n,m) circumferential and axial half waves

$$p_{\mathrm{crt},nm}=N_{\theta\theta 0,nm}/R=N_0\varepsilon_{b,nm}/R \tag{B.4}$$

The solution above is termed the "direct solution".

Since the linear stability (B1) including initial static displacement are inhomogeneous, a solution utilizing the Galerkin method is outlined in what follows. Expand displacement in terms of the dynamic eigenfunctions of the operator matrix (1a) that excludes time dependence and ε_b terms

$$\mathbf{G}_{sG}=\sum_{n}\sum_{m}a_{nm}\mathbf{\Phi}_{nm}(\theta)\mathbf{\Psi}_m(x) \tag{B.5}$$

(B.5) is similar to (12) with the coupling coefficients a_{nm} independent of t. Substituting (B.5) in (B.1a) noting that $\mathbf{\Phi}_{nm}(\theta)$ satisfy the dynamic Eq. (1a), enforcing orthogonality of $\mathbf{\Phi}_{nm}(\theta)$ and $\mathbf{\Psi}_m(x)$, then adding the three equations yields the coupled explicit eigenmatrix

$$\begin{aligned}&[-\mathbf{M}\lambda+\mathbf{K}_b]\mathbf{a}=\mathbf{0}\\&M_{il}=\delta_{ni}\delta_{ml}\omega_{nm}^2N_{nm},\quad \lambda=1/\varepsilon_b\\&N_{nm}=0.5\rho hRl_x\int_0^{\theta_l}(\varphi_{nm}^2+\eta_{nm}^2+\zeta_{nm}^2+\tilde{r}^2\chi((Rk_{xm}\zeta_{nm})^2+(\partial_\theta\zeta_{nm}-\eta_{nm})^2))\mathrm{d}\theta\end{aligned} \tag{B.6}$$

$\{\varphi,\eta,\zeta\}_{nm}$ are components of the displacement eigenvector, δ_{il} is the Kronecker delta, and $()'$ is derivative w.r.t. θ. Since $w_0(x,\theta)$ can be expressed as (see (4b) and (4c))

$$w_0(x,\theta)=\sum_{q=1}\zeta_{0q}(\theta)\sin(k_{xq}x)=\sum_{q=1}\sum_{k=1}^{8}w_{0kq}\mathrm{e}^{\alpha_{kq}\theta}\sin(k_{xq}x) \tag{B.7}$$

then the coefficients of $\mathbf{K}_b$ simplify to

$$\begin{aligned} K_{b,nm,il} &= (N_0/R^2)N_{1,nm,il} + (N_0/R^2)^2 N_{2,nm,il} \\ N_{1,nm,il} &= 0.5\delta_{ml} R l_x \int_0^{\theta_l} \zeta''_{il}\zeta_{nm}\,\mathrm{d}\theta \\ N_{2,nm,il} &= R\sum_{q=1}\int_0^{\theta_l}(\eta'_{il} - \zeta_{il} - vRk_{xl}\varphi_{il})\zeta_{nm}\zeta''_{0q}\,\mathrm{d}\theta \int_0^{l_x} \sin(k_{xm}x)\sin(k_{xl}x)\sin(k_{xq}x)\mathrm{d}x \end{aligned} \tag{B.8}$$

All the integrals in (B.8) are performed analytically since the integrands are either exponential or trigonometric functions.

References

Ambur, R., Starnes, J., Stoumbos, T., Kapania, R., 1995. Influence of large-deflection effects on the impact response of flat and curved composite plates, AIAA/ASME/ASCE/AHS/ASC. In: Structures, Structural Dynamics and Materials Conference, 36th, New Orleans, LA, April 10–12.

Blevins, R., 1981. Natural frequencies of shallow cylindrical curved panels. Journal of Sound and Vibration 75 (1), 145–149.

Byun, C., Kapania, R., 1992. Nonlinear impact response of thin imperfect laminated plates using a reduction method. Composite Engineering 2 (5–7), 391–410.

Chun, L., Lam, K., 1995. Dynamic analysis of clamped laminated curved panels. Composite Structures 30 (4), 389–398.

De Rosa, M., Franciosi, C., 2000. Exact and approximate dynamic analysis of circular arches using DQM. International Journal of Solids and Structures 37 (8), 1103–1117.

El-Raheb, M., 2006. Transient response of a thin cylinder with local material inhomogeneity, International Journal of Solids and Structures, in press, doi: 10.1016/j.ijsolstr.2005.04.041.

Johnson, E., Hyer, M.W., Carper, D.M., 1984. Response of long shallow cylindrical panels to radial line loads, AIAA 25th Structures. In: Structural Dynamics and Materials Conference, Palm Springs, CA, May 14–16, pp. 310–321.

Kapania, R., Stoumbos, T., 1994. Geometrically nonlinear impact response of thin laminated imperfect cylindrical panels. Composites Engineering 4 (4).

Kistler, L., Waas, A., 1999. On the response of curved laminated panels subjected to transverse impact loads. International Journal of Solids and Structures 36 (9), 1311–1327.

Matsuhashi, H., Graves, M., Dugundji, J., Lagace, P., 1993. Effect of membrane stiffening in transient impact analysis of composite laminated panels. In: Proceedings of the 34 AIAA/ASME/ASCE/AHS/ASC SDM, AIAA Hq., Washington, DC, pp. 2668–2678.

Mindlin, R., 1951. Influence of rotary inertia and shear deformation on flexural motions of isotropic elastic disks. Transactions of the ASME, Journal of Applied Mechanics 73, 31–38.

Prasad, C., Ambur, D., Starnes, J., 1994. Response of laminated composite plates to low-speed impact by different impactors. AIAA Journal 32 (6), 1270–1277.

Ramkumar, R., Thakar, Y., 1985. Dynamic response of curved laminated plates subjected to low velocity impact, ASME, Winter Annual Meeting, Miami Beach, FL, November 17–21.

Sheinman, I., Reichman, Y., 1992. A study of buckling and vibration of laminated shallow curved panels. International Journal of Solids and Structures 29 (11), 1329–1338.

Skvortsov, V., Bozhevolnaya, E., Kildegaard, A., 1998. Assessment of models for analysis of singly-curved sandwich panel. Composite Structures 41 (3–4), 289–299.

Skvortsov, V., Bozhevolnaya, E., Kildegaard, A., 2000. Overall behaviour of singly curved sandwich panels: the case of general boundary conditions. Composite Structures 49 (1), 95–109.